




# The Measles Virus V Protein Binding Site to STAT2 Overlaps That of IRF9

Yuma Nagano,<sup>a</sup> Aoi Sugiyama,<sup>b</sup> Madoka Kimoto,<sup>b</sup> Takuya Wakahara,<sup>a</sup> Yasuyo Noguchi,<sup>b</sup> Xinxin Jiang,<sup>a</sup> Shinya Saijo,<sup>c</sup> Nobutaka Shimizu,<sup>c</sup> Nana Yabuno,<sup>b</sup> Min Yao,<sup>b</sup> Paul R. Gooley,<sup>d,e</sup> Gregory W. Moseley,<sup>f</sup> Takashi Tadokoro,<sup>a</sup> Katsumi Maenaka,<sup>a,g</sup>  Toyoyuki Ose<sup>a,b,h</sup>

<sup>a</sup>Faculty of Pharmaceutical Sciences, Hokkaido University, Sapporo, Japan

<sup>b</sup>Faculty of Advanced Life Science, Hokkaido University, Sapporo, Japan

<sup>c</sup>Photon Factory, Institute of Materials Structure Science, High Energy Accelerator Research Organization (KEK), Tsukuba, Japan

<sup>d</sup>Department of Biochemistry and Molecular Biology, University of Melbourne, Parkville, Victoria, Australia

<sup>e</sup>Bio21 Molecular Science and Biotechnology Institute, University of Melbourne, Parkville, Victoria, Australia

<sup>f</sup>Department of Microbiology, Biomedicine Discovery Institute, Monash University, Victoria, Australia

<sup>g</sup>Global Station for Biosurfaces and Drug Discovery, Center for Life Innovation, Hokkaido University

<sup>h</sup>PRESTO, Japan Science and Technology Agency, Tokyo, Japan

**ABSTRACT** Measles virus (MeV) is a highly immunotropic and contagious pathogen that can even diminish preexisting antibodies and remains a major cause of childhood morbidity and mortality worldwide despite the availability of effective vaccines. MeV is one of the most extensively studied viruses with respect to the mechanisms of JAK-STAT antagonism. Of the three proteins translated from the MeV *P* gene, P and V are essential for inactivation of this pathway. However, the lack of data from direct analyses of the underlying interactions means that the detailed molecular mechanism of antagonism remains unresolved. Here, we prepared recombinant MeV V protein, which is responsible for human JAK-STAT antagonism, and a panel of variants, enabling the biophysical characterization of V protein, including direct V/STAT1 and V/STAT2 interaction assays. Unambiguous direct interactions between the host and viral factors, in the absence of other factors such as Jak1 or Tyk2, were observed, and the dissociation constants were quantified for the first time. Our data indicate that interactions between the C-terminal region of V and STAT2 is 1 order of magnitude stronger than that of the N-terminal region of V and STAT1. We also clarified that these interactions are completely independent of each other. Moreover, results of size exclusion chromatography demonstrated that addition of MeV-V displaces STAT2-core, a rigid region of STAT2 lacking the N- and C-terminal domains, from preformed complexes of STAT2-core/IRF-associated domain (IRF9). These results provide a novel model whereby MeV-V can not only inhibit the STAT2/IRF9 interaction but also disrupt preassembled interferon-stimulated gene factor 3.

**IMPORTANCE** To evade host immunity, many pathogenic viruses inactivate host Janus kinase signal transducer and activator of transcription (STAT) signaling pathways using diverse strategies. Measles virus utilizes P and V proteins to counteract this signaling pathway. Data derived largely from cell-based assays have indicated several amino acid residues of P and V proteins as important. However, biophysical properties of V protein or its direct interaction with STAT molecules using purified proteins have not been studied. We have developed novel molecular tools enabling us to identify a novel molecular mechanism for immune evasion whereby V protein disrupts critical immune complexes, providing a clear strategy by which measles virus can suppress interferon-mediated antiviral gene expression.

**KEYWORDS** STAT transcription factors, immune evasion, innate immunity, measles, paramyxovirus, protein purification, protein-protein interactions, recombinant-protein production, structural biology, zinc finger proteins

**Citation** Nagano Y, Sugiyama A, Kimoto M, Wakahara T, Noguchi Y, Jiang X, Saijo S, Shimizu N, Yabuno N, Yao M, Gooley PR, Moseley GW, Tadokoro T, Maenaka K, Ose T. 2020. The measles virus V protein binding site to STAT2 overlaps that of IRF9. *J Virol* 94:e01169-20. <https://doi.org/10.1128/JVI.01169-20>.

**Editor** Susana López, Instituto de Biotecnología/UNAM

**Copyright** © 2020 American Society for Microbiology. All Rights Reserved.

Address correspondence to Toyoyuki Ose, [ose.toyoyuki@sci.hokudai.ac.jp](mailto:ose.toyoyuki@sci.hokudai.ac.jp).

**Received** 9 June 2020

**Accepted** 13 June 2020

**Accepted manuscript posted online** 24 June 2020

**Published** 17 August 2020

The interferon (IFN) system, including type I (primarily IFN- $\alpha/\beta$ ) and type II (IFN- $\gamma$ ), which are critical to the development of innate and adaptive immune responses against viral infection, is known to be targeted by many pathogenic viruses. In the type I pathway, together with interferon regulatory factor 9 (IRF9), STAT1 and STAT2 form a heterotrimer called interferon-stimulated gene factor 3 (ISGF3), which translocates to the nucleus to bind to a specific sequence called the interferon-stimulated response element (ISRE), present in promoter regions of interferon-stimulated genes (ISGs). Some of the best-studied viruses antagonizing the type I pathway are in the family *Paramyxoviridae*, including the genus *Morbillivirus* (such as measles virus [MeV]), the genus *Rubulavirus* (such as mumps virus), the genus *Henipaviruses* (such as Nipah virus [NiV] and Hendra virus), the genus *Respirovirus* (such as Sendai virus), and the genus *Avulavirus* (such as Newcastle disease virus) (1). The *P* gene in the paramyxovirus genome can encode multiple proteins (including P, V, W, D, I, and C proteins), which variously function as antagonists of the IFN pathways. The expression of distinct protein isoforms from the *P* gene relies on an RNA-editing mechanism as well as the use of alternate open reading frames within the *P* gene. In the former, the insertion of one or more guanosines into the *P* gene mRNA transcripts at a predetermined editing site generates two or three different proteins (P, V, and W/D/I) sharing the N-terminal sequences but with distinct C-terminal sequences (2–4) (Fig. 1A). In the latter, translation from an internal start codon in an alternative reading frame results in the expression of one or more C proteins (2, 5, 6).

Measles, for which no therapeutic agents are currently available, remains a major cause of childhood morbidity and mortality worldwide, being responsible for up to 100,000 deaths annually despite the availability of effective vaccines (7). MeV, the causative agent, has a nonsegmented negative-strand RNA genome of approximately 16 kb. Morbilliviruses also include *Canine distemper virus*, *Rinderpest virus*, *peste des petits ruminants virus*, *Cetacean morbillivirus*, *Feline morbillivirus*, and *Phocine distemper virus*. MeV infection induces profound immunosuppression that is connected to secondary infections and mortality (8). The MeV *P* gene is translated into three proteins: P, an essential polymerase cofactor, and V and C, which have been reported to possess multiple functions but are not essential for virus propagation in cultured cells (9, 10). MeV P (MeV-P) and V (MeV-V) proteins have been reported to antagonize the type I and/or type II IFN pathways, although the precise mechanism of inhibition at the molecular level is not fully defined, largely due to a lack of direct analysis of the underlying molecular interactions. Although the IFN type I pathway is regarded as the main target of MeV-V (11–14), there are reports that the MeV-V protein interferes with the type II IFN pathway depending on cell type and the expression level of MeV-V (14–16). Inhibition of STAT1/STAT2 nuclear translocation has been observed in the presence of MeV-V upon IFN stimulation (14, 15, 17). In addition, blockade of STAT1 phosphorylation has been reported: inactivation of Tyk2 phosphorylation was identified in MeV-V-expressing cells (16), whereas blockade of Jak1 was observed by another group (13), which is consistent with observations in MeV-infected cells (18). Pulldown assays have demonstrated that MeV-V can interact with STAT1, STAT2, IRF9, and Jak1 (13, 15), although it is not clear if the interaction is direct.

In the absence of any complex structure for MeV-V with STAT1 and STAT2 (and/or with IRF9), the molecular basis of inactivation of type I/II IFN signaling by MeV-V is incompletely understood. However, several studies have provided some insights. Nuclear magnetic resonance (NMR) data showed that MeV-V N termini (amino acids 1 to 231; MeV-V<sub>NT</sub>, equivalent to MeV-P<sub>NT</sub>) is an intrinsically disordered protein (IDP) (19). Cell-based yeast two-hybrid, pulldown/coimmunoprecipitation, and reporter gene signaling assays indicate that both the V<sub>NT</sub> (P<sub>NT</sub>) and the C termini (amino acids 232 to 299; V<sub>CT</sub> region [Fig. 1]) are important for inactivation of the IFN- $\alpha/\beta$  signaling pathway, and other studies show that P<sub>NT</sub> is the region that interacts with STAT1 (13, 14, 17, 20–22). Caignard et al. identified a MeV-P<sub>NT</sub> peptide encompassing amino acids 110 to 120 (<sub>110</sub>YHVYDHSGEAV<sub>120</sub>) as the key region that interacts with STAT1, with a contribution by a MeV-P<sub>NT</sub> peptide encompassing amino acids 121 to 231 (17). Important residues

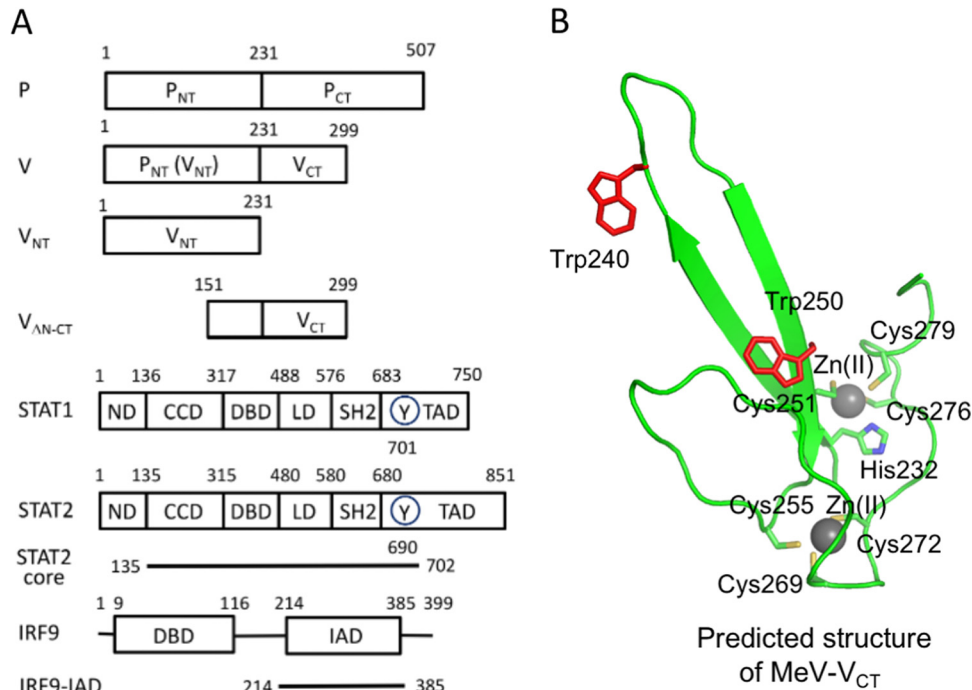


**FIG 1** (A) Schematic illustrating the open reading frames and domain organization of P, V, STAT1, STAT2, and IRF9. P<sub>NT</sub>, P N-terminal domain; P<sub>CT</sub>, P C-terminal domain; ND, N-terminal domain; CCD, coiled-coil domain; DBD, DNA-binding domain; LD, linker domain; SH2, Src homology domain; TAD, transactivation domain; IAD, IRF-association domain. Tyr701 and Tyr690, which are phosphorylated to activate STAT1 and STAT2, respectively, are indicated by a circle. The designed constructs of STAT2-core and IRF9-IAD are indicated as bars below each molecule. (B) MeV-V<sub>CT</sub> structure predicted model using SWISS-MODEL (50) based on PIV (PDB ID 2B5L). The predicted two zinc ions are shown as gray spheres. The two tryptophan residues (Trp240 and Trp250) that we mutated and that have been reported to be important for the inhibition of the IFN type I pathway in cell-based assays (17) are shown in red.

in STAT1 for MeV-P<sub>NT</sub> interaction were in turn mapped based on the capacity of specific mutations to prevent antagonism by MeV-P of STAT1 phosphorylation and nuclear translocation (23). The MeV-V<sub>CT</sub>/STAT2 interaction is also well characterized. In contrast to the V<sub>NT</sub> (P<sub>NT</sub>), which is highly divergent between paramyxoviruses, the amino acid sequence of V<sub>CT</sub> is approximately 50% identical among all paramyxovirus V proteins. Crystal structures are available for the V<sub>CT</sub> of parainfluenza virus 5 (PIV5) in complex with ubiquitin ligase DDB1 and the helicase domain of melanoma differentiation associated protein-5 (24, 25). These have indicated two zinc atoms, which are predicted to coordinate the conserved single histidine and seven cysteine residues in MeV-V<sub>CT</sub> (26, 27) (Fig. 1B). The important residues for the function of MeV-V<sub>CT</sub> have been studied; in particular, Trp240, Phe246, Asp248, and Trp250 were identified as crucial for the interaction with STAT2 (14, 17). However, since neither the free form nor a complex form of the three-dimensional MeV-V structure is known, a complete understanding of its IFN/STAT-antagonistic mechanism is lacking.

To enable direct evaluation of critical molecular interactions in MeV-V function, we established a protocol for molecular production and analysis of MeV-V. To our knowledge, this is the first study to purify MeV-V and MeV-V<sub>CT</sub>, enabling us to perform detailed biophysical analyses of interactions *in vitro* to reveal new mechanistic data. In addition to the preparation of host factors such as STAT1 (nonphosphorylated and phosphorylated forms), STAT2, and IRF9 IRF-associated domain (IRF9-IAD), we observed and quantified unambiguous direct interactions between MeV-V/STAT1 and MeV-V/STAT2 for the first time. In addition to STAT1 and STAT2, which contain an N domain (ND), a coiled-coil domain (CCD), a DNA binding domain (DBD), a linker domain (LD), an SH2 domain, and a C-terminal transactivation domain (TAD) (Fig. 1A), we prepared a STAT2-core, which is a central rigid region without ND and TAD. Consequently, we were

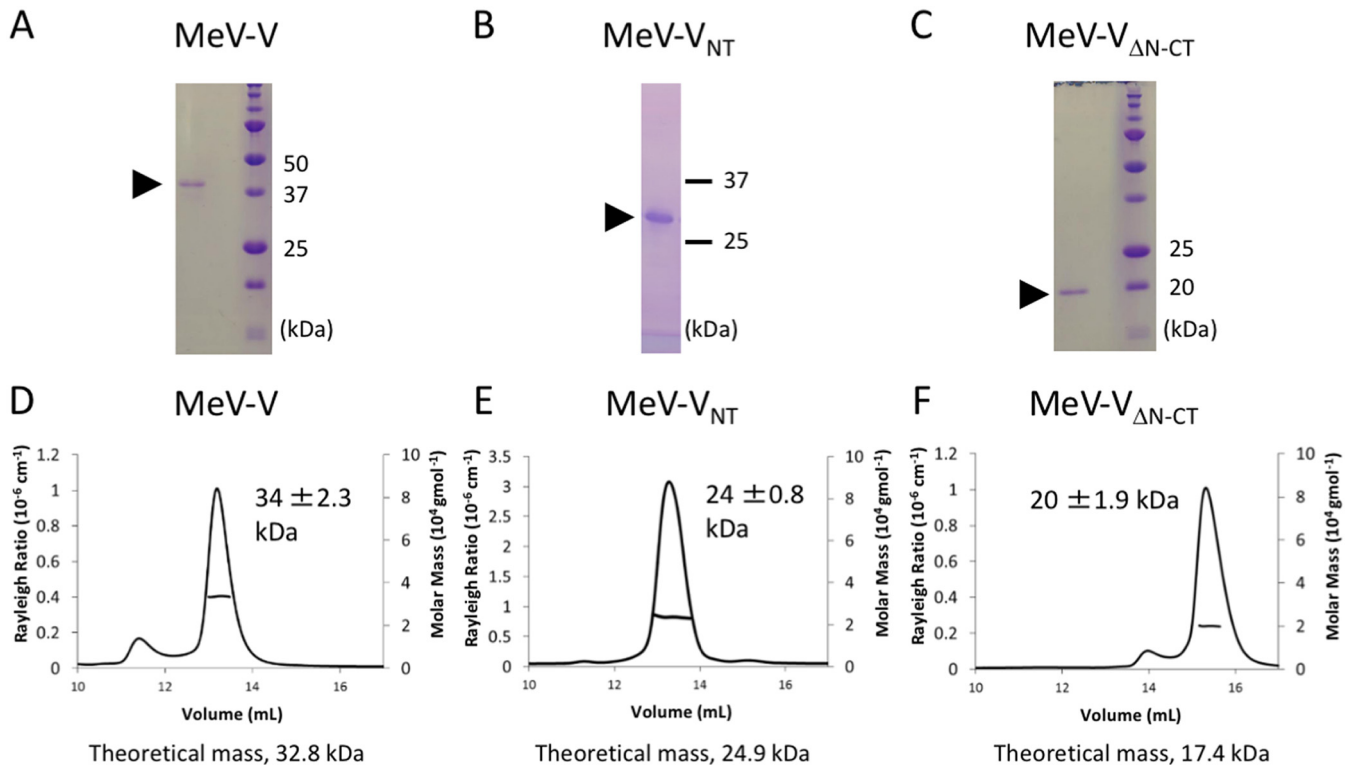


**FIG 2** SDS-PAGE analysis of purified MeV-V (A), MeV-V<sub>NT</sub> (B), and MeV-V<sub>ΔN-CT</sub> (C). Proteins were separated in a 15% acrylamide gel and stained with Coomassie brilliant blue. SEC-MALS profiles of V protein variants are shown in MeV-V (D), MeV-V<sub>NT</sub> (E), and MeV-V<sub>ΔN-CT</sub> (F), with the scattering strength indicated by the black line and the left axis and the averaged molecular mass indicated by the black line and right axis. The values in each frame,  $\pm$  error, are the estimated molecular masses at peak position analyzed by using ASTRA analysis software package (Wyatt Technology). The theoretical mass of each monomer is at the bottom of each chromatogram.

able to directly monitor that binding of MeV-V and IRF9-IAD to STAT2-core is competitive, such that MeV-V disrupts a preformed STAT2-core/IRF9-IAD interaction, suggesting a new potential mechanism by which MeV-V protein can prevent type I IFN signaling by preventing ISGF3 formation.

## RESULTS

**MeV-V has a large intrinsically disordered region and a zinc finger motif.** To the best of our knowledge, although bacterial recombinant expression was successful (26, 28), no report has previously described biophysical characterization of purified MeV-V except that for MeV-V<sub>NT</sub> (19). We selected glutathione *S*-transferase (GST) as a solubility enhancer tag to prepare MeV-V protein because the N-terminal region has been reported to be intrinsically disordered by NMR (19). We attempted to express recombinant MeV-V, MeV-V<sub>NT</sub> (amino acids 1 to 231, common region with MeV-P), and MeV-V<sub>CT</sub> separately in bacteria. On sequence comparison, MeV-V<sub>CT</sub> is expected to comprise amino acids 232 to 299 (Fig. 1A) (14, 17). The zinc finger motif in MeV-V<sub>CT</sub> is predicted using the crystal structure of V protein from PIV5 (24, 25) (Fig. 1B). We successfully expressed MeV-V and MeV-V<sub>NT</sub> using *Escherichia coli* BL21 Star (DE3). However, we were not able to prepare MeV-V<sub>CT</sub> due to a low expression level using the same system in bacteria. Therefore, the construct with amino acids 151 to 299, termed MeV-V<sub>ΔN-CT</sub> (Fig. 1A), was used for expression after screening different N-terminal truncations experimentally. We successfully purified these MeV-V variants by GST-affinity column chromatography and GST removal using 3C protease on beads, followed by size exclusion chromatography (SEC). The purity and yield of all the proteins generated (MeV-V, MeV-V<sub>NT</sub> [amino acids 1 to 231], MeV-V<sub>ΔN-CT</sub> [amino acids 151 to 299], MeV-V W240A, and MeV-V W250A) were sufficient for further assays (Fig. 2A to C).

To characterize the proteins, we used several methods. First, we used multiangle static light scattering (MALS) coupled with SEC (SEC-MALS) to evaluate the oligomerization state. The interpolation using the Zimm plot (29) of the major fractions from the SEC demonstrated that the estimated molecular masses from MALS are  $34 \pm 2.3$  kDa for MeV-V,  $24 \pm 0.8$  kDa for MeV-V<sub>NT</sub>, and  $20 \pm 1.9$  kDa for MeV-V<sub>ΔN-CT</sub> (Fig. 2D to F), which shows good agreement with the theoretical values of monomers, i.e., 32.8 kD for MeV-V, 24.9 kDa for MeV-V<sub>NT</sub>, and 17.4 kDa for MeV-V<sub>ΔN-CT</sub>. This result indicated that MeV-V, MeV-V<sub>NT</sub>, and MeV-V<sub>ΔN-CT</sub> homogeneously exist as monomers in solution. Second, we analyzed the size of the molecules using small-angle X-ray scattering (SAXS) combined with SEC (SEC-SAXS). The Guinier plot and the normalized Kratky plot were calculated to estimate the protein size and judge the folding of the protein. The details of the SAXS experiment results are given in Table 1. Using the  $Q$  ( $4\pi\sin\theta/\lambda$ ;  $\lambda$ , wavelength) range described in Table 1, the radius of gyration ( $R_g$ ) from the Guinier plot and the normalized Kratky plot was calculated to investigate the folding of the protein (30). The normalized Kratky plots demonstrated that MeV-V<sub>ΔN-CT</sub> is partially disordered and MeV-V and MeV-V<sub>NT</sub> are mostly disordered. The plot of MeV-V<sub>ΔN-CT</sub> has a small peak in the small-angle region, indicating that a part of the protein is folded (Fig. 3). The Guinier analysis gave the  $R_g$  values of 51.1 Å for MeV-V, 45.1 Å for MeV-V<sub>NT</sub>, and 36.4 Å for MeV-V<sub>ΔN-CT</sub>. The molecular weights were also calculated on the basis of the intensity of forward scattering [ $I(0)$ ] values from the Guinier analysis, i.e., 35.7 kDa for MeV-V, 28.7 kDa for MeV-V<sub>NT</sub>, and 19.4 kDa for MeV-V<sub>ΔN-CT</sub>. These values correlated well with the theoretical mass values based on amino acid sequences and the results of SEC-MALS (Fig. 2).  $R_g$  values are based on the approximate relationship of molecular mass ( $M$ ) and volume ( $V$ ) for a protein ( $M$  [daltons] =  $825 V$  [nm<sup>3</sup>]), and the minimal radius ( $R_{\min}$ ) of a sphere of this volume that could contain the given mass of globular protein can be calculated [ $R_{\min} = (3V/4\pi)^{1/3} = 0.066 M^{1/3}$  (where  $R_{\min}$  is in nanometers)] (31). Using the following relationship of  $R_g$  and radius ( $R$ ), and assuming the object to be a sphere,

$$R_g = \sqrt{\frac{3}{5}}R$$

the minimal  $R_g$  values of each MeV-V variant can be estimated to be 16.2 Å for MeV-V, 14.8 Å for MeV-V<sub>NT</sub>, and 13.0 Å for MeV-V<sub>ΔN-CT</sub> using the theoretical molecular masses for MeV-V, MeV-V<sub>NT</sub>, and MeV-V<sub>ΔN-CT</sub>. The values from the Guinier analyses (MeV-V, 51.1 Å; MeV-V<sub>NT</sub>, 45.1 Å; MeV-V<sub>ΔN-CT</sub>, 36.4 Å) are much bigger than those of the theoretical values when the proteins are assumed to be spherical (MeV-V, 16.2 Å; MeV-V<sub>NT</sub>, 14.8 Å; MeV-V<sub>ΔN-CT</sub>, 13.0 Å). As the proteins appear as monomers in solution, based on the MALS results (Fig. 2), the  $R_g$  values from the Guinier analysis and the normalized Kratky plot suggest that the proteins are not globular and compact particles. Third, we focused on the predicted zinc finger motif in MeV-V<sub>CT</sub> (Fig. 1B). The zinc binding ability of recombinant MeV-V (full length) has already been experimentally confirmed using the <sup>65</sup>Zn blotting method from bacterial lysate (26). Since the affinity of a Zn ion(s) has not been analyzed and the loss of a Zn ion(s) during the purification procedure is possible, the confirmation of the presence of Zn is necessary. Here, for MeV-V and MeV-V<sub>ΔN-CT</sub>, the presence of a zinc ion(s) was identified by the typical K absorption edge wavelength of Zn approximately 1.2837 Å from the X-ray absorption fine structure (XAFS) by using synchrotron radiation (Fig. 4). We can thus conclude that the zinc finger domain is encompassed in these purified recombinant proteins as predicted.

**Characterization of recombinant (phosphorylated and unphosphorylated) STAT1 and STAT2.** In general, previous biochemical and structural characterizations of STAT proteins have used mainly truncated proteins (the N-terminal domain or the core domain [Fig. 1]) (32–35). The N-terminal domain (ND) and the transactivation domain (TAD) are connected to the core region by short flexible linkers (Fig. 1). As the effect of truncation on MeV-V interaction is unknown, we established a protocol to generate full-length STAT1 and STAT2 to analyze the interaction with the viral protein. As MeV-V has been shown to interact with both human STAT1 and human STAT2 (14, 17), we

**TABLE 1** SAXS data collection and analysis of measles virus protein variants MeV-V, MeV-V<sub>ΔN-CT</sub>, and MeV-V<sub>NT</sub>

Parameter	Data or value for:		
	MeV-V	MeV-V <sub>NT</sub>	MeV-V <sub>ΔN-CT</sub>
<b>Sample details</b>			
Extinction coefficient ( $A_{280nm}$ , $Abs_{0.1\%}$ [wt/vol])	0.852	0.401	1.117
Partial specific vol ( $\bar{v}$ ) ( $cm^3 g^{-1}$ )	0.722	0.720	0.729
Mean scattering contrast ( $\Delta\rho \times 10^{10}$ ) ( $cm^{-2}$ )	3.076	3.007	2.870
$M$ from chemical composition (Da)	32,821	24,862	17,445
Concn ( $mg ml^{-1}$ ) <sup>a</sup>	0.397	0.537	1.140
<b>SAXS data collection parameters</b>			
Source	Photon Factory	Photon Factory	Photon Factory
Instrument	BL-15A2	BL-10C	BL-15A2
Wavelength (Å)	1.213	1.000	1.213
Camera length (mm)	2,563	2,009	1,562
Beam geometry ( $\mu m$ )	V140 × H540 K/B mirror + 2 slits + 1 pinhole	V350 × H550 Bent cylindrical mirror + 2 slits + 1 pinhole	V90 × H550 K/B mirror + 2 slits + 1 pinhole
Detector	PILATUS3 2M (Dectris)	PILATUS3 2M (Dectris)	PILATUS3 2M (Dectris)
$q$ measurement range ( $\text{Å}^{-1}$ )	0.049–0.259	0.070–0.402	0.068–0.425
Absolute scaling method	Comparison with scattering from pure H <sub>2</sub> O	Comparison with scattering from pure H <sub>2</sub> O	Comparison with scattering from pure H <sub>2</sub> O
Basis for normalization to constant counts	Normalized to incident intensity by $\mu$ ion chamber	Normalized to incident intensity by $\mu$ ion chamber	Normalized to incident intensity by $\mu$ ion chamber
Method for monitoring radiation damage	Data frame-by-frame comparison	Data frame-by-frame comparison	Data frame-by-frame comparison
Exposure time (s)	10	20	10
Sample temp (K)	293	293	293
Flow rate of HPLC during exposure (ml/min)	0.10	0.05	0.10
<b>Guinier analysis</b>			
$R_g$ (Å)	51.1 ± 0.3	45.1 ± 0.7	36.4 ± 0.1
$I(0)$ ( $cm^{-1}$ )	0.0223 ± 0.0001	0.0231 ± 0.0002	0.0302 ± 0.0001
$M$ from $I(0)$	35,751	28,650	19,368
$Q$ range	0.0059–0.0254	0.0081–0.0285	0.0097–0.0354
$Q \times R_g$ range	0.30–1.30	0.36–1.28	0.35–1.29
<b>Software for SAXS data analysis (reference)</b>			
SAXS data processing	Sangler (47)	Sangler (47)	Sangler (47)
Guinier analysis	autorg of ATSAS (48)	autorg of ATSAS (48)	autorg of ATSAS (48)
Calculation of $\epsilon$ from sequence	ExpASY (51)	ExpASY (51)	ExpASY (51)
Calculation of $\Delta\rho$ and $\bar{v}$ values	MULCh (52)	MULCh (52)	MULCh (52)

<sup>a</sup>Protein sample concentration was evaluated by UV-visible spectroscopy at the SAXS sample position using a solvent composed of 10 mM HEPES-NaOH, 150 mM NaCl, and 1 mM DTT, pH 7.4.

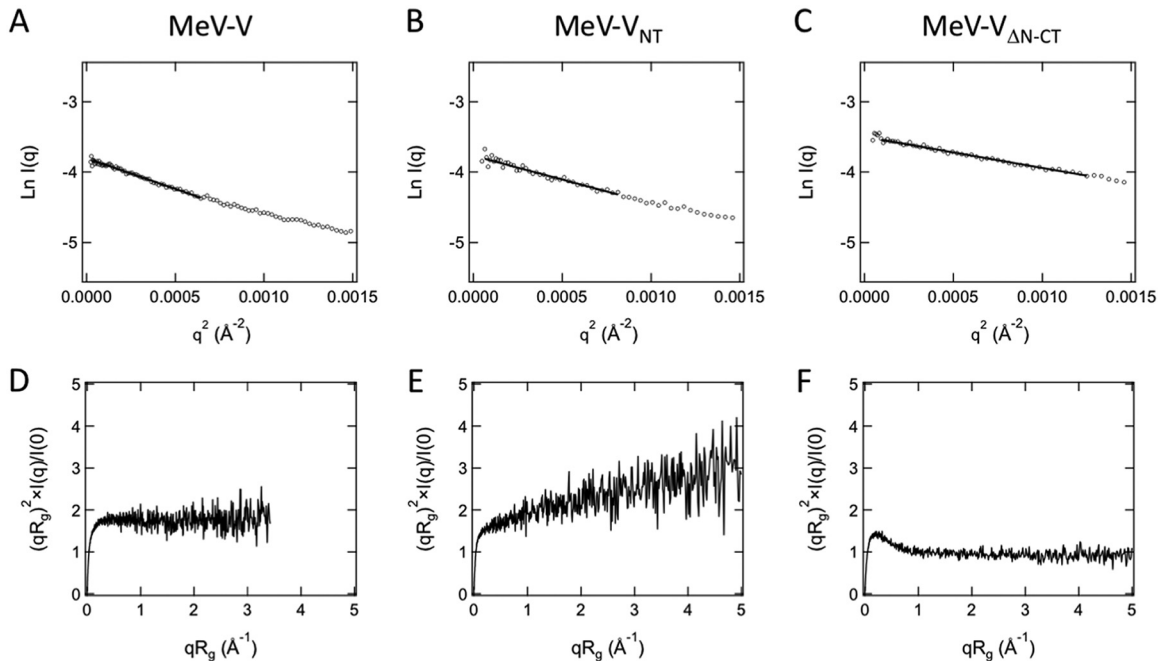


**FIG 3** SAXS analyses of MeV-V protein variants. Guinier plots are shown for MeV-V (A), MeV-V<sub>NT</sub> (B), and MeV-V<sub>ΔN-CT</sub> (C). Normalized Kratky plots are shown for MeV-V (D), MeV-V<sub>NT</sub> (E), and MeV-V<sub>ΔN-CT</sub> (F).

prepared several STAT1 and STAT2 constructs, including full-length and phosphorylated forms, in *E. coli*. We first produced unphosphorylated human STAT1 (full-length U-STAT1) with an N-terminal GST tag or N-terminal 6×His tag; however, these constructs were unsuccessful due to low yield, aggregation, and fragmentation. On the other hand, U-STAT1 with the protein GB1 domain (GB1) fusion tag followed by a 6×His tag as a solubility enhancer (36, 37) was highly soluble. The purity and oligomerization state of U-STAT1 were further assessed using SDS-PAGE and SEC-MALS (Fig. 5A). The SEC showed two peaks, where the second peak is dimeric U-STAT1 eluting with a molecular mass of  $187 \pm 28$  kDa (theoretical mass, 176 kDa). The N-terminal domain of STAT1 was reported to mediate dimer formation (32, 38); therefore, these results

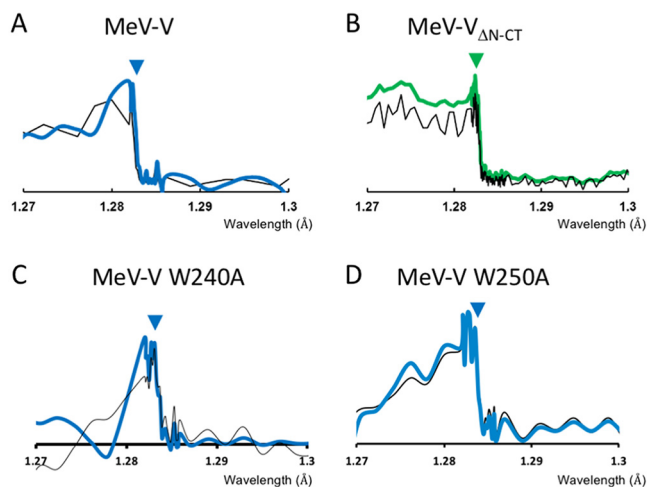


**FIG 4** X-ray fluorescence analysis to identify the X-ray absorption fine structure (XAFS). The photon count of the fluorescence X-ray over the incident photon is plotted against the wavelength (thin lines). The target functions estimated by CHOCH (49) from the fluorescence data are indicated by thick lines. (A) MeV-V; (B) MeV-V<sub>ΔN-CT</sub>; (C) MeV-V W240A; (D) MeV-V W250A.

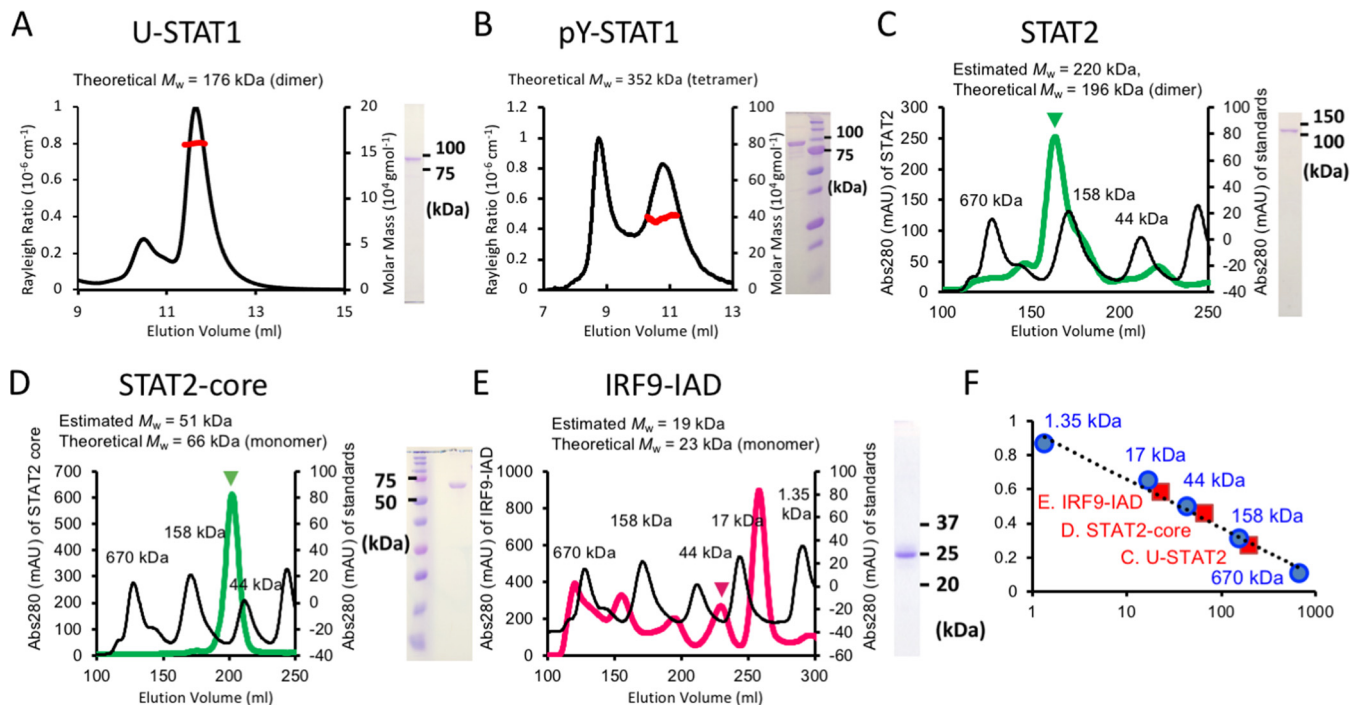


**FIG 5** Chromatogram and SDS-PAGE analysis of STAT1 (A), pY-STAT1 dimer (B), full-length STAT2 (C), STAT2-core region (D), and IRF9-IAD (E). (A and B) SEC-MALS profiles are shown, with the scattering strength indicated by the black line and left axis and the averaged molecular mass indicated by the red line and right axis. (C to E) The elution positions of the target proteins are indicated by inverted triangles. All of the chromatograms are overlaid with the elution pattern of standard proteins of (i) 670 kDa (thyroglobulin), (ii) 158 kDa (gamma globulin), (iii) 44 kDa (ovalbumin), (iv) 17 kDa (myoglobin), and (v) 1.35 kDa (vitamin B<sub>12</sub>). The chromatograms of the standards are indicated by horizontal black lines using the scale of the right axes. (F) A calibration curve was plotted using the gel-phase distribution coefficient ( $K_{av}$ ) versus the logarithm of the molecular weight ( $\log M_w$ ).  $K_{av} = (V_e - V_o)/(V_c - V_o)$ , where  $V_e$  is the elution volume,  $V_o$  is the column void volume (105.1 ml), and  $V_c$  is the column bed volume (318.6 ml). The straight line was calculated by the least-squares method from the data for molecular weight standards ( $R^2 = 0.981$ ) shown in blue circles. Red squares correspond to the positions of  $K_{av}$  values for the purified proteins indicated in panels C to E as described above. The equation  $Y = -0.125 \times \log X + 0.9463$  from the calibration line was used to calculate the experimental molecular weights shown at the bottom of the chromatograms in panels C to E.

suggest that unphosphorylated STAT1 is present as a dimer that is connected via the N-terminal domains.

To obtain tyrosine 701-phosphorylated STAT1 (pY-STAT1) in *E. coli* BL21(DE3) TKB1, we did not have to use GB1, since the N-terminal 6×His tag alone was sufficient for homogeneous purification. The SEC showed the elution signal of pY-STAT1 with two peaks, the first peak corresponding to a soluble aggregate of pY-STAT1. The second peak, analyzed by SEC-MALS, corresponds to pY-STAT1 eluting with a molecular mass of  $390 \pm 66$  kDa, which approximately corresponds to a tetramer (theoretical mass, 352 kDa) (Fig. 5B). Tetramer formation of pY-STAT1 is likely due to an interaction between the phosphotyrosine 701 and SH2 domains of opposing STATs, in addition to the interactions via the N-terminal domain. The fractions containing the dimer peak of U-STAT1 and the tetramer peak of pY-STAT1 were used for binding assays.

The purity of human unphosphorylated full-length STAT2 and STAT2-core is shown in Fig. 5C and D. Using the standard curve of the SEC column, the elution positions of full-length STAT2 and the STAT2-core region were 163.2 ml and 202.2 ml, respectively, equivalent to molecular masses of 220 kDa and 51 kDa (Fig. 5C to E). This result indicates that full-length STAT2 is a dimer (theoretical mass, 196 kDa) and the STAT2-core is a monomer (theoretical mass, 66 kDa), consistent with the report that similar to STAT1, the dimerization of STAT2 is mediated by the N-terminal domain (39). We could not purify Tyr680-phosphorylated STAT2 (pY-STAT2) because of instability; thus, the binding assay between pY-STAT2/MeV-V and pY-STAT1/pY-STAT2/MeV-V will remain as future work.

**MeV-V binds to unphosphorylated STAT1 via the N-terminal domain.** The direct interactions between MeV-V and STAT proteins have not been quantified. We per-



formed isothermal titration calorimetry (ITC) experiments to evaluate the molecular interactions between the viral protein and the host proteins. Because STAT1/2 proteins aggregated on concentration, MeV-V proteins were used as the injectant for ITC after concentration.

First, we assayed the interaction of the MeV-V variants and unphosphorylated STAT1 (U-STAT1). The U-STAT1/MeV-V combination gave an exothermic profile of one-site binding with an  $N$  (stoichiometry) value of  $1.1 \pm 0.4$  (Fig. 6A; Table 2). The  $N$  value was derived from the monomer concentrations of all MeV-V and STAT variants. The dissociation constant ( $K_D$ ) of the interaction is  $5.7 \pm 0.5 \mu\text{M}$ , determined by two independent experiments and calculated to fit well with a 1:1 binding model. This interaction is mainly enthalpy driven with a small favorable entropy ( $\Delta G = -6.90 \pm 0.02 \text{ kcal/mol}$ ,  $\Delta H = -6.5 \pm 2.4 \text{ kcal/mol}$ , and  $-T\Delta S = -0.47 \pm 2.4 \text{ kcal/mol}$ ; where  $\Delta H$  is enthalpy change and  $\Delta S$  is entropy change). The thermodynamic profile of U-STAT1/MeV-V<sub>NT</sub> (amino acids 1 to 231) was similar to that of U-STAT1/MeV-V (Fig. 6B), showing a  $K_D$  value of  $9.3 \pm 4.5 \mu\text{M}$  that is enthalpy driven with a favorable entropy change ( $\Delta G = -6.7 \pm 0.3 \text{ kcal/mol}$ ,  $\Delta H = -5.6 \pm 1.2 \text{ kcal/mol}$ ,  $-T\Delta S = -1.1 \pm 1.6 \text{ kcal/mol}$ , and stoichiometry  $N = 1.1 \pm 0.4$ ). As U-STAT1/V<sub>ΔN-CT</sub> (amino acids 151 to 299) provided no heat generation by the ITC experiment (Fig. 6C; Table 2), we concluded that the MeV-V<sub>NT</sub> region is a main contributor to recognition of U-STAT1 in the U-STAT1/MeV-V interaction. The important region in MeV-V<sub>NT</sub> to interact with STAT1 (either unphosphorylated or phosphorylated) (17), <sub>110</sub>YHVYDHSGEAV<sub>120r</sub>, comprises several polar and hydrophobic residues. Therefore, the enthalpy-driven interaction with STAT1 may come from interactions of the polar residues, and the small difference of entropy between MeV-V and MeV-V<sub>NT</sub> may be explained by the mobility of the MeV-V<sub>NT</sub> not being affected after binding and/or hydrophobic interactions are included. Next, we tested whether MeV-V<sub>NT</sub> targets pY-STAT1 by using ITC. As shown in Fig. 6D, no heat generation was observed, suggesting that MeV-V does not bind pY-STAT1, which is likely due to the conformational change that occurs on phosphorylation.

**MeV-V binds to STAT2 via V<sub>ΔN-CT</sub> and binding to STAT2 is stronger than to STAT1.** We next examined combinations of STAT2 and MeV-V variants by ITC. The dissociation constant ( $K_D$ ) of the STAT2/MeV-V interaction is  $0.18 \pm 0.1 \mu\text{M}$ , determined by two independent experiments and calculated to fit well with a 1:1 binding model ( $N$  value of  $1.2 \pm 0.1$ ) (Fig. 6E). This interaction is also enthalpy driven with a small entropy change (Table 2) ( $\Delta G = -8.9 \pm 0.3 \text{ kcal/mol}$ ,  $\Delta H = -9.3 \pm 2.0 \text{ kcal/mol}$ , and  $-T\Delta S = 0.38 \pm 1.7 \text{ kcal/mol}$ ). Heat generation was not observed from the STAT2/MeV-V<sub>NT</sub> combination (Fig. 6F). On the other hand, the thermodynamic profile of STAT2/MeV-V<sub>ΔN-CT</sub> (amino acids 151 to 299) is comparable to that of STAT2/MeV-V (Fig. 6G); the  $K_D$  value is  $0.13 \pm 0.02 \mu\text{M}$  when enthalpy driven, but with an unfavorable entropy change (Table 2) ( $\Delta G = -9.0 \pm 0.3 \text{ kcal/mol}$ ,  $\Delta H = -12.0 \pm 0.7 \text{ kcal/mol}$ ,  $-T\Delta S = 2.6 \pm 0.8 \text{ kcal/mol}$ , and stoichiometry  $N = 1.2 \pm 0.1$ ). Therefore, MeV-V<sub>ΔN-CT</sub> is responsible for STAT2 binding. Importantly, the interaction between MeV-V and STAT2 ( $K_D = 0.18 \pm 0.1 \mu\text{M}$ ) was more than 30 times stronger than that between MeV-V and STAT1 ( $K_D = 5.7 \pm 0.5 \mu\text{M}$ ) (Fig. 6A and E).

To clarify which region of STAT2 is targeted by MeV-V (MeV-V<sub>ΔN-CT</sub>), the STAT2-core (Fig. 1, amino acids 135 to 702) was subjected to ITC experiments with MeV-V, MeV-V<sub>NT</sub>, and MeV-V<sub>ΔN-CT</sub>. The  $K_D$  value of the STAT2-core/MeV-V interaction is  $0.25 \pm 0.2 \mu\text{M}$  (Fig. 6H), from two independent experiments and a 1:1 binding model, with an  $N$  value of  $1.0 \pm 0.1$ . This interaction is enthalpy driven with a small unfavorable entropy change ( $\Delta G = -8.8 \pm 0.6 \text{ kcal/mol}$ ,  $\Delta H = -9.9 \pm 0.4 \text{ kcal/mol}$ , and  $-T\Delta S = 1.1 \pm 0.2 \text{ kcal/mol}$ ). No heat generation was detected with the combination of STAT2-core/MeV-V<sub>NT</sub> (Fig. 6I), whereas the  $K_D$  value of the STAT2-core/MeV-V<sub>ΔN-CT</sub> interaction was  $0.08 \pm 0.06 \mu\text{M}$  (Fig. 6J), from two independent experiments and a 1:1 binding model, with an  $N$  value of  $1.1 \pm 0.1$ . This interaction is enthalpy driven with a small unfavorable entropy change ( $\Delta G = -9.4 \pm 0.6 \text{ kcal/mol}$ ,  $\Delta H = -11.6 \pm 0.7 \text{ kcal/mol}$ , and  $-T\Delta S = 2.2 \pm 1.3 \text{ kcal/mol}$ ). These experiments show that STAT2-core and MeV-V<sub>ΔN-CT</sub> are the key components of the MeV-V/STAT2 interaction. All the  $K_D$  and thermodynamic

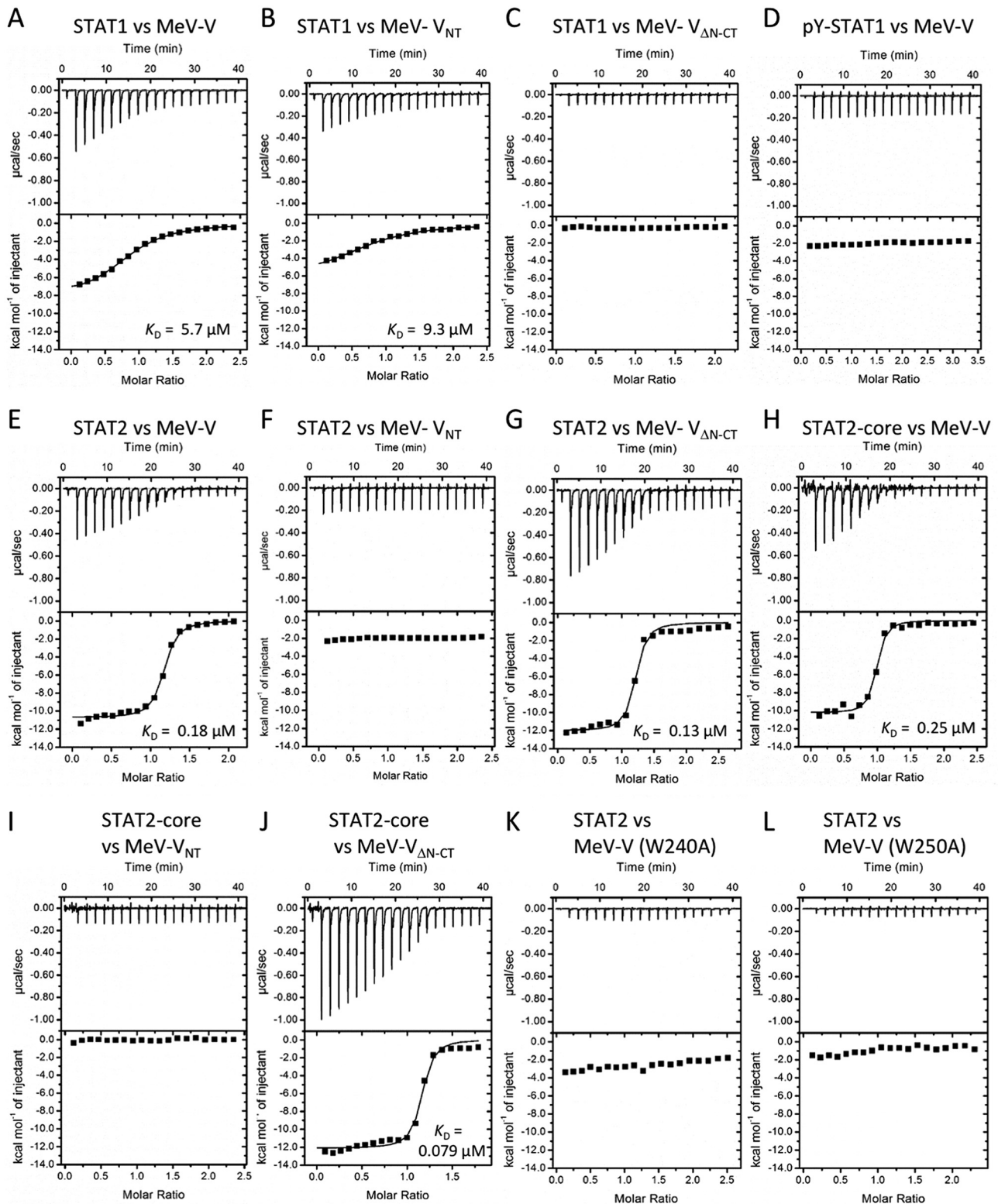


**FIG 6** (A to D) ITC measurements for MeV-V protein variants binding to U-STAT1 and pY-STAT1. The upper panels show the representative titration thermograms after blank value subtraction, and the lower panels show the data integration with fitted curves (1:1 binding model): U-STAT1 dimer with MeV-V ( $K_D = 5.7 \mu\text{M}$ ) (A), MeV-V<sub>NT</sub> binding ( $K_D = 9.3 \mu\text{M}$ ) (B), and MeV-V<sub>ΔN-CT</sub> (no binding) (C), and pY-STAT1 tetramer with MeV-V (no binding) (D). (E to L) ITC measurements for MeV-V protein variants binding to STAT2. The upper panels show the representative titration thermograms after blank value subtraction, and the lower panels show the data integration with fitted curves (1:1 binding model): STAT2 with MeV-V ( $K_D = 0.18 \mu\text{M}$ ) (E), MeV-V<sub>NT</sub> (no binding) (F), and MeV-V<sub>ΔN-CT</sub> ( $K_D = 0.13 \mu\text{M}$ ) (G); STAT2-core region with MeV-V ( $K_D = 0.25 \mu\text{M}$ ) (H), MeV-V<sub>NT</sub> (no binding) (I), and MeV-V<sub>ΔN-CT</sub> ( $K_D = 0.079 \mu\text{M}$ ) (J); STAT2 with MeV-V W240A (no binding) (K) and MeV-V W250A (no binding) (L).

**TABLE 2**  $K_D$  values and other thermodynamic parameters of each binding interaction quantified by ITC<sup>a</sup>

Combination	$K_D$ ( $\mu\text{M}$ )	Stoichiometry	$\Delta G$ (kcal/mol)	$\Delta H$ (kcal/mol)	$-T\Delta S$ (kcal/mol)
STAT1 vs MeV-V	$5.7 \pm 0.5$	$1.1 \pm 0.4$	$-6.9 \pm 0.02$	$-6.5 \pm 2.4$	$-0.47 \pm 2.4$
STAT1 vs MeV-V <sub>NT</sub>	$9.3 \pm 4.5$	$1.1 \pm 0.4$	$-6.7 \pm 0.3$	$-5.6 \pm 1.2$	$-1.1 \pm 1.6$
STAT1 vs MeV-V <sub><math>\Delta\text{N-CT}</math></sub>	No heat generation	No heat generation	No heat generation	No heat generation	No heat generation
pY-STAT1 vs MeV-V	No heat generation	No heat generation	No heat generation	No heat generation	No heat generation
STAT2 vs MeV-V	$0.18 \pm 0.1$	$1.2 \pm 0.1$	$-8.9 \pm 0.3$	$-9.3 \pm 2.0$	$0.38 \pm 1.7$
STAT2 vs MeV-V W240A	No heat generation	No heat generation	No heat generation	No heat generation	No heat generation
STAT2 vs MeV-V W250A	No heat generation	No heat generation	No heat generation	No heat generation	No heat generation
STAT2 vs MeV-V <sub>NT</sub>	No heat generation	No heat generation	No heat generation	No heat generation	No heat generation
STAT2 vs MeV-V <sub><math>\Delta\text{N-CT}</math></sub>	$0.13 \pm 0.02$	$1.2 \pm 0.1$	$-9.0 \pm 0.3$	$-12.0 \pm 0.7$	$2.6 \pm 0.8$
STAT2-core vs MeV-V	$0.25 \pm 0.2$	$1.0 \pm 0.09$	$-8.8 \pm 0.6$	$-9.9 \pm 0.4$	$1.1 \pm 0.2$
STAT2-core vs MeV-V <sub>NT</sub>	No heat generation	No heat generation	No heat generation	No heat generation	No heat generation
STAT2-core vs MeV-V <sub><math>\Delta\text{N-CT}</math></sub>	$0.079 \pm 0.06$	$1.1 \pm 0.007$	$-9.4 \pm 0.6$	$-11.6 \pm 0.7$	$2.2 \pm 1.3$
STAT2-core vs IRF9-IAD	$0.24 \pm 0.07$	$1.1 \pm 0.06$	$-8.7 \pm 0.3$	$-9.1 \pm 0.9$	$0.34 \pm 1.1$
MeV-V vs IRF9-IAD	No heat generation	No heat generation	No heat generation	No heat generation	No heat generation

<sup>a</sup>The experiments were carried out at 15°C and pH 7.4.

parameters are summarized in Table 2. These data quantified in solution expand on the previously observed results in cell-based assays, such as yeast two-hybrid, coimmunoprecipitation, and pulldown assays (13, 14, 17).

We also evaluated the STAT2 interaction using MeV-V mutants. Of the four reported important residues in MeV-V<sub>CT</sub> (Trp240, Phe246, Asp248, and Trp250) (14, 17), we prepared two MeV-V mutants, i.e., MeV-V W240A and MeV-V W250A. ITC experiments with these mutants demonstrated that the interaction between MeV-V and STAT2 was abolished (Fig. 6K and L), in agreement with data from a previous cell-based reporter gene assay (17). In the homology model of MeV-V<sub>CT</sub> (Fig. 1B), the two tryptophan residues are located on the  $\beta$ -hairpin: Trp240 is located on a loop between the two  $\beta$ -strands, and Trp250 is on the second  $\beta$ -strand. The XAFS measurement was also carried out for MeV-V W240A and MeV-V W250A (Fig. 4); the data show that the zinc finger motif is not disrupted, and therefore the two Trp residues likely contribute to the interaction of MeV-V with STAT2. Together with the report that Phe246 and Asp248 are also important for a MeV-V<sub>CT</sub> function reporter gene assay (14), these data indicate that the  $\beta$ -hairpin plays an important role in the enthalpy-driven interaction with the STAT2-core (Fig. 1B). The findings that the thermodynamic profiles of MeV-V/STAT2 (STAT2/MeV-V, STAT2/MeV-V <sub>$\Delta\text{N-CT}$</sub> , and STAT2-core/MeV-V <sub>$\Delta\text{N-CT}$</sub> ) are similar and are all enthalpy driven with small unfavorable entropy changes suggest that the interaction is essentially driven by the formation of the polar/ionic interface with little loss of mobility.

**MeV-V <sub>$\Delta\text{N-CT}$</sub>  interferes with STAT2/IRF9 binding.** As MeV-V <sub>$\Delta\text{N-CT}$</sub>  interacts specifically with the STAT2-core, we sought to assess whether the MeV-V <sub>$\Delta\text{N-CT}$</sub>  binding region of STAT2 overlaps the IRF9 binding region recently revealed by crystallography (40). In this structure, the IRF-associated domain of human IRF9 (IRF9-IAD) interacts with the coiled-coil domain (CCD) of STAT2 (40) (Fig. 1). To test whether MeV-V <sub>$\Delta\text{N-CT}$</sub>  competes with IRF9-IAD for STAT2, we prepared IRF9-IAD by following a method reported previously (40). The SEC profile is shown in Fig. 5E, where the elution volume of IRF9-IAD (229.1 ml) corresponds to a molecular mass of 18.6 kDa (Fig. 5D and E), indicating that IRF9-IAD is monomeric (theoretical mass, 23 kDa).

The specific interaction between the STAT2-core and IRF9-IAD was evaluated using ITC and gave a  $K_D$  value of  $0.24 \pm 0.07 \mu\text{M}$ . The interaction is enthalpy driven, with a small unfavorable entropy change (Table 2; Fig. 7A) ( $\Delta G = -8.7 \pm 0.3 \text{ kcal/mol}$ ,  $\Delta H = -9.1 \pm 0.9 \text{ kcal/mol}$ ,  $-T\Delta S = 0.34 \pm 1.1 \text{ kcal/mol}$ , and stoichiometry  $N = 1.1 \pm 0.1$ ). The  $K_D$  value of the STAT2-core and IRF9-IAD interaction derived from our experiment is higher than that previously reported using ITC ( $K_D = 0.01 \mu\text{M}$ ), probably because of the difference in experimental conditions. No significant heat generation was observed for the titration of IRF IAD on MeV-V (Fig. 7B); thus, IRF IAD is not a target of MeV-V.

To analyze whether the MeV-V/STAT2-core interaction affects the STAT2-core/IRF9-IAD binding, which could prevent ISGF3 formation, competition experiments were

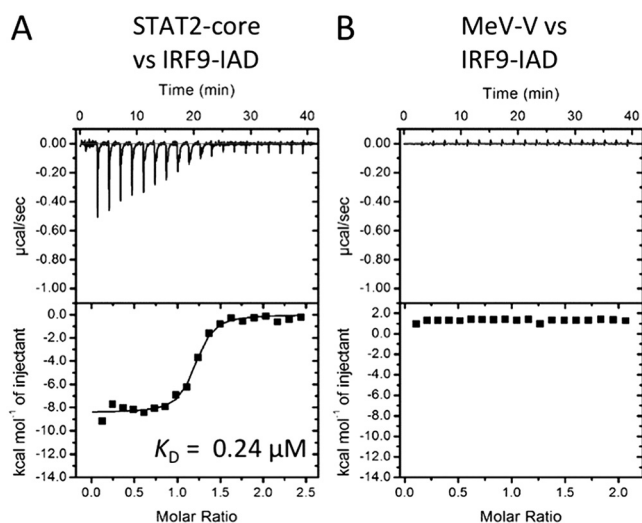


**FIG 7** ITC measurements for the interaction between MeV-V protein and STAT2-core ( $K_D = 0.24 \mu\text{M}$ ) (A) and IRF9-IAD (no binding) (B). The upper panels show representative titration thermograms after blank value subtraction, and the lower panels show the data integration with fitted curves (1:1 binding model).

performed by surface plasmon resonance (SPR). The response from the binding of IRF9-IAD and the STAT2-core was monitored using IRF9-IAD immobilized on a CAP chip. We injected 50 nM STAT2-core in the absence of MeV-V (Fig. 8A). Next, we injected 50 nM STAT2-core in the presence of MeV-V (1 to 5  $\mu\text{M}$ ) and showed a dose-dependent competition (Fig. 8A).

The SPR-based inhibition assay (described above) showed real-time but imperfect inhibition of STAT2/IRF9 binding by MeV-V (Fig. 8A). Since both STAT2-core/IRF9-IAD and STAT2-core/MeV-V binary complexes can be observed by size exclusion chromatography (Fig. 8B), we tried to assess the effect of MeV-V addition (4.8  $\mu\text{M}$ ) onto a preformed STAT2-core/IRF9-IAD complex (1:1 molar ratio, 4.8  $\mu\text{M}$ ) in the injectant (1:1:1 mixture) (Fig. 8B and C). It was observed that the signal intensity corresponding to the STAT2-core/MeV-V complex from injection of the 1:1:1 mixture (25.4 milliabsorbance units [mAU] at 11.9 ml) is comparable to that from injection of STAT2-core/MeV-V in a 1:1 mixture (28.1 mAU at 11.8 ml) (Fig. 8B). There was little signal observed at the IRF9-IAD peak position (15.6 ml) (Fig. 8B) from the STAT2-core/IRF9-IAD 1:1 mixture; however, there was clear peak of IRF9-IAD from the 1:1:1 mixture (4.0 mAU at 15.6 ml) (Fig. 8B and C). An elution profile from the MeV-V/IRF9-IAD 1:1 mixture (4.0  $\mu\text{M}$  each) showed that there is no interaction between the two molecules; the values of the peak intensity (MeV-V, 8.7 mAU at 13.2 ml; IRF9-IAD, 6.6 mAU at 15.8 ml) were almost identical to the values from independent MeV-V and IRF9-IAD injections (MeV-V, 8.7 mAU at 13.3 ml; IRF9-IAD, 6.6 mAU at 15.9 ml) (Fig. 8D). SDS-PAGE analysis of the elution from the 1:1:1 mixture confirmed the presence of both STAT2-core/MeV-V (Fig. 8B and E, lanes 2 to 4) and STAT2/IRF9-IAD (Fig. 8B and E, lanes 5 and 6) complexes with expelled free IRF9-IAD (Fig. 8B, C, and E, lane 10). Therefore, we concluded that formation of comparable amounts of the STAT2-core/MeV-V complex and the STAT2-core/IRF9-IAD complex appeared when MeV-V was added to the preexisting STAT2-core/IRF9-IAD complex, consistent with MeV-V displacing IRF9-IAD from STAT2.

## DISCUSSION

Characterization of the direct interactions between viral proteins and host defense factors is necessary for understanding the viral immunosuppression mechanism and for the control and prevention of the disease. Strategies to control current significant human pathogens and/or to prepare for potential threats of other morbilliviruses to human or animal populations in the future (for example, canine distemper virus [41]) will be greatly facilitated by understanding the molecular basis of pathogenesis.

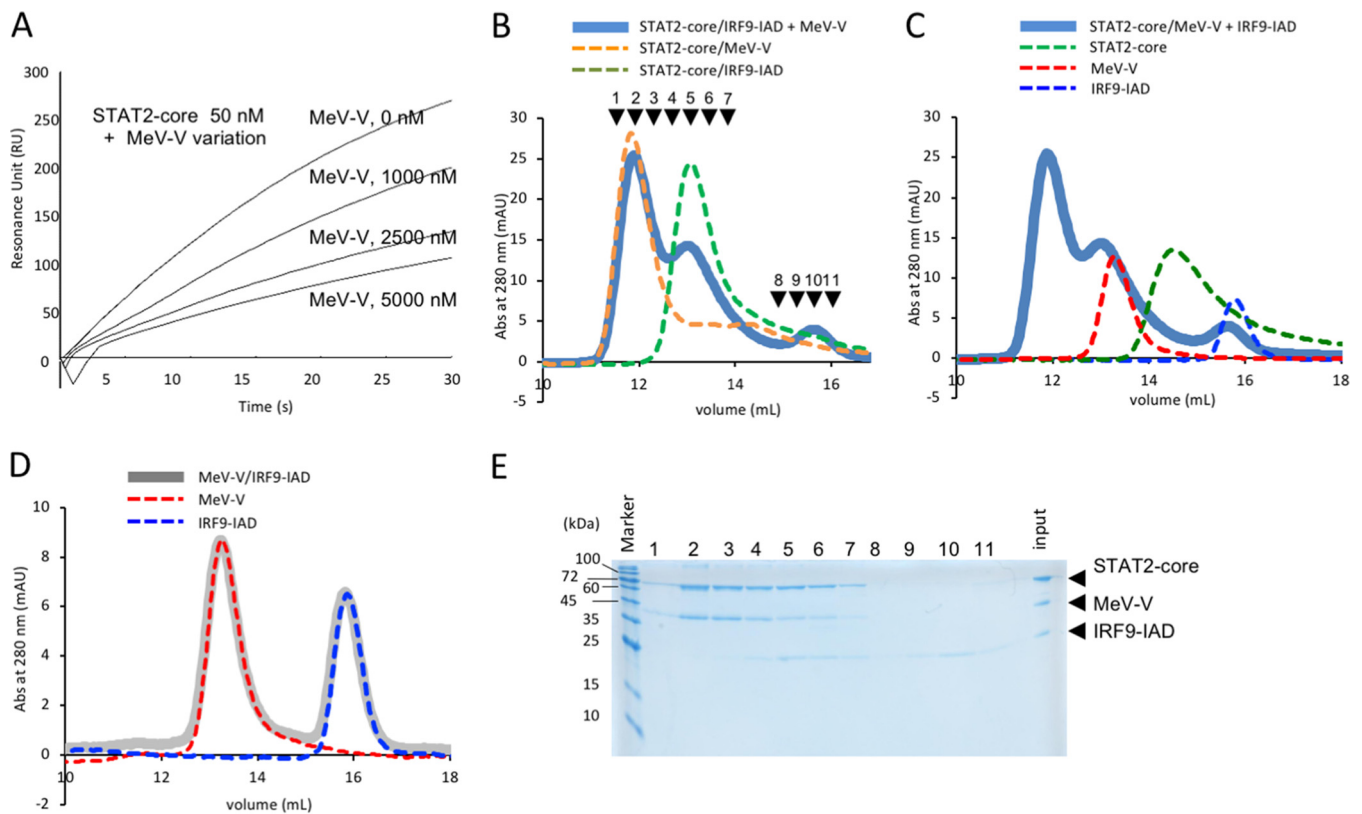


**FIG 8** (A) Inhibition assay of STAT2-core/IRF9-IAD binding by MeV-V using SPR. A 50 nM concentration of STAT2-core was injected in the presence of 0 to 5,000 nM MeV-V on an IRF9-IAD immobilized chip. The detection was at 2 Hz. (B) Complex formation analysis using size exclusion chromatography. Elution of the STAT2-core/MeV-V plus IRF9-IAD mixture (1:1:1) is represented by a bold blue line. The STAT2-core/MeV-V mixture (1:1 ratio) and STAT2-core/IRF9-IAD mixture (1:1 ratio) are represented by a dashed orange line and a green line, respectively. (C) Complex formation analysis using size exclusion chromatography. Elution of the STAT2-core/MeV-V plus IRF9-IAD mixture (1:1:1) is represented by a bold blue line (the same as for panel B). STAT2-core, MeV-V, and IRF9-IAD are represented by dashed green, red, and blue lines, respectively. Arrows with numbers indicate fractions from the 1:1:1 mixture analyzed by SDS-PAGE in panel E. (D) Elution of the MeV-V/IRF9-IAD mixture (1:1) is represented by a bold gray line. MeV-V and IRF9-IAD are represented by dashed red and blue lines, respectively. (E) SDS-PAGE analysis of the elution of the STAT2-core/MeV-V plus IRF9-IAD mixture (1:1:1) as described for panel B. The lane numbers correspond to the numbers indicated in panel B. The positions of STAT2-core (66 kDa), MeV-V (32.8 kDa), and IRF9-IAD (23 kDa) bands are indicated on the right.

The important regions in MeV-V, including MeV-V<sub>NT</sub> and MeV-V<sub>CT</sub>, that interact with STAT1 or STAT2 have been studied using cell-based assays (13, 14, 16, 17, 20–22). However, fundamental aspects of these interactions, including whether they are direct, are not understood, and, importantly, the molecular basis by which these interactions result in inactivation of the type I or type II IFN systems is unclear. Furthermore, in the reported data regarding the interaction of MeV-V with host molecules, there are some discrepancies. Some groups demonstrated that MeV-V can block the type II IFN pathway (14–16, 21), but this is not always the case (11). Different results were also observed concerning the prevention of JAK kinase phosphorylation. Blockade of Tyk2 phosphorylation was identified in MeV-V-expressing cells (16), whereas blockade of Jak1 was observed by another group (13), and the latter observation was consistent with data in MeV-V-infected cells (18). The debate on the aforementioned contradictions indicated that virus strain, cell types, and protein expression levels can affect the results; nevertheless, the data indicate that the formation of complexes of MeV-V with Jak1/Tyk2 or STAT1/STAT2 is likely (16, 18). The difficulty in distinguishing between direct and indirect interactions by cell-based assays such as the yeast two-hybrid assay and coimmunoprecipitation means that other methods are required to delineate these mechanisms.

To precisely understand these events, we evaluated the interactions of STAT1/2, MeV-V, and IRF9-IAD by biophysical methods using purified proteins. Based on the ability of MeV-V to interact with both STAT1 and STAT2, it is generally accepted that

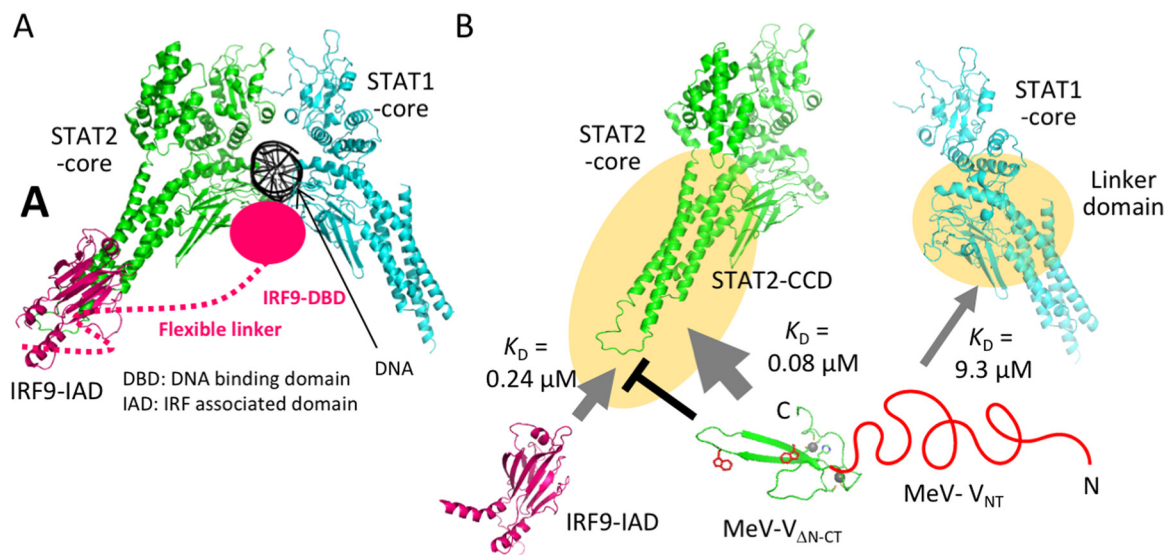


**FIG 9** (A) Interferon-stimulated gene factor 3 (ISGF3) and DNA-binding model based on the crystal structures of pY-STAT1 DNA (PDB ID 1BF5) (35) and STAT2-core/IRF9 IAD (PDB ID 5OEN) (40). (B) Model of the inhibition of ISGF3 formation by MeV-V from the ITC and SPR experiments. The  $K_D$  values between each minimum component revealed in this study are shown. The information that MeV-V $_{NT}$  targets the linker domain of STAT1 (23) was also used.

MeV-V mainly targets several processes of the ternary complex formed by phosphorylated STAT1/STAT2 and IRF9 (ISGF3) in the type I IFN signaling pathway, although an inhibition of type II IFN signaling pathway has also been reported (14–16). Our ITC data revealed that the interaction of MeV-V and STAT1 is 30-fold weaker than that of MeV-V and STAT2 (Fig. 6). This result can clearly explain why the main target of MeV-V might be the inhibition of ISGF3 formation rather than homodimer formation of phosphorylated STAT1, called the gamma activated factor (GAF), as suggested by more consistent data for the former in the literature (11–14). A typical example is a report that efficient STAT1 binding in cells depends on the presence of STAT2 (14), which may be interpreted as indicating that direct STAT1-V interaction is not stable enough to be maintained in cells in the absence of STAT2. However, Devaux et al. showed that STAT1-blind recombinant MeV is attenuated in rhesus monkeys and elicits a stronger immune response than the wild-type MeV (22). To explain the molecular basis of this phenomenon, we will probably have to consider the effect of other factors, such as inactivation of Jak1 and Tyk2, which would form the basis of important future work. Since MeV-V is a STAT binder, we show that MeV-V/STAT interactions can be divided into two components, MeV-V $_{NT}$ /STAT1 and MeV-V $_{\Delta N-CT}$ /STAT2, without any cross-interaction (Fig. 9B). MeV-V $_{NT}$ , shown here empirically and reported previously (19) to be an intrinsically disordered region (IDR), does not require MeV-V $_{CT}$  to interact with STAT1. IDRs are hypothesized to adapt to multiple targets while keeping specificity and affinity (42). In fact, previously, the importance of the ability of MeV-V $_{NT}$  (and MeV-P $_{NT}$ ) to bind to the Jak1 kinase domain to inhibit phosphorylation of STAT1 was investigated by yeast two-hybrid and pulldown assays in HEK293T cells, and different regions of MeV-V $_{NT}$  were reported to interact with STAT1 and Jak1 (13).

In the STAT1 structure, the linker and the SH2 domains have been reported to control the interaction with MeV-P $_{NT}$  in U3A cells (23). Using an as yet unresolved mechanism, probably involving inhibition of multiple targets of the consecutive phosphorylation cascade from Jak1 to STAT1, MeV-V $_{NT}$  (and MeV-P $_{NT}$ ) can block STAT1 phosphorylation. Intrinsic disorder properties are possibly useful to bind several targets, as can be seen in other intrinsically disordered proteins. A mechanism for the inhibition of STAT1 phosphorylation by Sendai virus C protein (SeV-C) was suggested based on the crystal structure of SeV-C in complex with the ND of STAT1 (38). Because SeV-C

targets a different region of STAT1 (the ND), the interference mechanism of STAT1 phosphorylation by MeV-V must be different at the molecular level. However, the possible inhibition strategy of MeV-V<sub>NT</sub>, by analogy to the SeV-C case, may involve blocking the transition of the STAT1 dimer from the antiparallel (unphosphorylated) to a parallel (phosphorylated) conformation, as suggested previously (38), which is also worthy of consideration. In fact, the present result that pY-STAT1 (a tetramer in solution) did not interact with MeV-V may imply that the MeV-V binding interface on STAT1 is important for the transition. Our method for evaluating the molecular interaction can be applied in the future to understand this viral strategy for inhibiting the phosphorylation of STAT1 molecules.

Our study focusing on the MeV-V<sub>ΔN-CT</sub>/STAT2-core interaction leads to one clear interpretation that MeV-V<sub>CT</sub> intervenes in ISGF3 formation. We identified the STAT2-core as the target region of MeV-V<sub>ΔN-CT</sub>, because the  $K_D$  between MeV-V<sub>ΔN-CT</sub> and the STAT2-core is almost the same as that between MeV-V<sub>ΔN-CT</sub> and full-length STAT2 (Table 2,  $0.08 \pm 0.06 \mu\text{M}$  and  $0.13 \pm 0.02 \mu\text{M}$ , respectively). The crystal structure of the STAT2 coiled-coil domain (CCD, amino acids 133 to 315) in complex with IRF9-IAD was presented recently (40). In that study, based on the complex structure and on the previously reported pY-STAT1 core dimer structure (35), the ISGF3 complex model bound to DNA was built (Fig. 9A) (40). In this model, the N-terminal DNA binding domains (DBD) of IRF9 and IRF9-IAD are connected by a flexible polypeptide linker. We investigated the possibility that MeV-V prevents IRF9/STAT2 binding. From our ITC and SEC experiments, we showed that there is no interaction between MeV-V and IRF9-IAD (Fig. 7 and 8D) and that the STAT2-core/IRF9-IAD interaction ( $K_D = 0.24 \pm 0.07 \mu\text{M}$ ) is comparable to that of the STAT2-core/MeV-V ( $K_D = 0.25 \pm 0.2 \mu\text{M}$ ). Using SPR, we further showed that the presence of MeV-V affects STAT2-core/IRF9-IAD binding in a dose-dependent manner (Fig. 8A). However, the real-time response monitored by SPR indicated that the effect of inhibition is small even in the presence of 100 times more MeV-V than STAT2-core (Fig. 8A). Then we analyzed the effect of MeV-V addition to a preformed STAT2-core/IRF9-IAD complex. In the presence of an equivalent molecular ratio of STAT2-core, MeV-V, and IRF9-IAD, the retention volume from the size exclusion column showed that the portion of the STAT2-core/MeV-V complex from the 1:1 mixture and the portion of the STAT2-core/MeV-V complex from the 1:1:1 mixture (addition of MeV-V into the preassembled STAT2-core/IRF9-IAD complex) are comparable; a significant portion of IRF9-IAD was expelled from the preassembled STAT2-core/IRF9-IAD complex (Fig. 8B). Although no interaction was observed between MeV-V and IRF9-IAD from our ITC and SEC experiments (Fig. 7B and 8D), the interaction of these molecules may be different on a STAT2 "platform." Nonetheless, from two independent experiments (SPR and SEC), our data clearly indicate that the IRF9-IAD binding region on the STAT2-core (40) should overlap the MeV-V binding region (Fig. 9).

As observed for other viral counteraction events targeting the JAK-STAT pathway, the molecular basis by which the type I and/or type II pathways are blocked has been difficult to examine because of the functional redundancy of each accessory protein. In this study, we clearly uncovered an antagonistic mechanism whereby disruption of the STAT2-core/IRF9-IAD interaction would impair ISRE gene expression. This is the first observation explaining how ISGF3 malfunction can be caused at the molecular level by measles virus.

## MATERIALS AND METHODS

**Protein purification of MeV-V, MeV-V<sub>NT</sub>, and MeV-V<sub>ΔN-CT</sub>.** cDNA coding for intact MeV-V, MeV-V<sub>NT</sub> (amino acids 1 to 231), and MeV-V<sub>ΔN-CT</sub> (amino acids 151 to 299) was introduced into pGEX6P-2 (GE Healthcare) using EcoRI and XhoI. To impair the expression of the C protein from the same cDNA (MeV-V and MeV-V<sub>NT</sub>), two stop codons were introduced immediately downstream of the C protein initiation codon without the influence of the amino acid sequence of the V protein, as reported previously (20). *Escherichia coli* strain BL21 Star (DE3) (Thermo Fisher Scientific) was transformed using each expression vector. A single colony of the transformant was inoculated into 100 ml of LB medium (with 30  $\mu\text{g/ml}$  of ampicillin) and incubated at 37°C and 180 rpm with shaking. Then, 6 ml of the preculture was inoculated into 1 liter of 2 $\times$  YT medium in 3-liter baffled flasks and shaken at 180 rpm at 37°C. IPTG (isopropyl- $\beta$ -

D-thiogalactopyranoside; 1 mM final concentration) was added when the culture reached an optical density at 600 nm ( $OD_{600}$ ) of 0.8, followed by incubation at 16°C for 24 h. The cells were washed twice with buffer A (10 mM Na phosphate, pH 7.4, 150 mM NaCl, 1 mM dithiothreitol [DTT], 10% glycerol). Finally, cells were harvested by centrifugation.

The cells were resuspended in 0.2 mg/ml (final concentration) of cell lysis buffer (buffer A, DNase I [Merck], hen egg lysozyme [Wako]) and disrupted using a sonicator. The cell solution was centrifuged at 10°C and  $40,000 \times g$  for 1 h, and the supernatant was collected. After filtration, glutathione Sepharose 4B (GE Healthcare) was added to the soluble fraction and resuspended overnight. After washing with buffer A, the MeV-V variants were eluted from the resin using GST-fused 3C protease in the presence of 5 mM DTT. The proteins were further purified via size exclusion chromatography using a HiLoad 26/60 Superdex 200 prep grade column equilibrated with buffer B {10 mM HEPES, pH 7.4, 150 mM NaCl, 1 mM TCEP [Tris(2-carboxyethyl)phosphine hydrochloride]}.

**Protein purification of human STAT1, STAT2, and IRF9-IAD.** cDNA coding for full-length STAT1, full-length STAT2, the core region of STAT2 (amino acids 136 to 702), and IRF9 IRF-associated domain (IRF9-IAD; amino acids 182 to 385) was inserted into pET21d (Merck) in fusion with an N-terminal 6 $\times$ His tag and GB1. *E. coli* B834 (DE3) was transformed with each vector. A chaperone expressing plasmid pGTF2 (TaKaRa; encoding GroEL, GroES, and Trigger factor) was used especially for the transformation with pET21d for full-length STAT2, the core region of STAT2, and IRF9-IAD. Bacterial cell culture, expression induction, and cell lysis were conducted as described for MeV-V expression. A chaperone expressing plasmid pGTF2 (encoding GroEL, GroES, and Trigger factor) was utilized especially for full-length STAT2 and the STAT2-core region, because the soluble fraction of cell lysates from these constructs without pGtf2 contained very little target protein. Column chromatography for these proteins was performed using similar methods. For the first Ni affinity chromatography, Ni-nitrilotriacetic acid (Ni-NTA) agarose (Qiagen) was used with the Ni-NTA binding buffer (20 mM Tris-HCl, pH 8.0, 150 mM NaCl, 20 mM imidazole). Ni-NTA elution buffer (20 mM Tris-HCl, pH 8.0, 150 mM NaCl, 250 mM imidazole) was used for elution from the resin. For STAT1, STAT2, and STAT2-core, an anion-exchange Resource Q 1-ml column (GE Healthcare) was used as the second column. The binding and wash buffer contains 10 mM Na phosphate, pH 8.0, 50 mM NaCl, and 1 mM TCEP. Elution was conducted using a linear gradient against the same buffer including 1.5 M NaCl. After removal of the His tag using 3C protease, the protein fraction was applied to size exclusion chromatography using a HiLoad 26/60 Superdex 200 prep grade column equilibrated with buffer B. To calculate the standard curve, the same buffer was used to analyze the elution volume of each protein included in a gel filtration standard (Bio-Rad; thyroglobulin [670 kDa], gamma globulin [158 kDa], ovalbumin [44 kDa], myoglobin [17 kDa], vitamin B<sub>12</sub> [1.35 kDa]) (Fig. 5).

**Protein purification of pY-STAT1.** To prepare tyrosine-phosphorylated STAT1 (pY-STAT1, N-terminally His tagged), a previously reported protocol (43) was followed. Briefly, *E. coli* BL21(DE3) TKB1 (Agilent Technologies), harboring a plasmid carrying the inducible tyrosine kinase gene (pTK), was used for the in-cell phosphorylation in the kinase buffer (1 $\times$  M9 medium supplemented with 0.1% [wt/vol] Casamino Acids [Wako], 1.5  $\mu$ M thiamine-HCl, 53  $\mu$ M 3 $\beta$ -indole acrylic acid). Column chromatography using HisTrap 5-ml (GE Healthcare), HiTrap heparin high-performance 5-ml (GE Healthcare), and HiLoad 26/60 Superdex 200 prep grade (GE Healthcare) columns was used.

**SEC-MALS.** Oligomerization of purified MeV-V, MeV-V<sub>NTT</sub>, and MeV-V<sub>AN-CT</sub> was analyzed by inline MALS combined with SEC (SEC-MALS) using the Alliance 2695 high-performance liquid chromatography (HPLC) system (Waters) coupled to a Dawn Heleos II MALS detector (Wyatt Technology) and 2414 refractive detector (Waters) to obtain the sample concentration. The absolute molecular mass was calculated by analyzing the scattering data using the ASTRA analysis software package (Wyatt Technology). Protein samples were applied after the separation using a Superdex 200 Increase 10/300 GL column (GE Healthcare) at a flow rate of 0.5 ml/min.

**SAXS data collection and processing.** SEC-SAXS data were obtained at the BL-10C (44) (MeV-V<sub>NTT</sub>) and BL15A2 (45) (MeV-V, MeV-V<sub>AN-CT</sub>), Photon Factory (Tsukuba, Japan). The Acquity UPLC H-class system (Waters) with a Superdex 200 Increase 10/300 GL column (GE Healthcare) was utilized to isolate each protein sample. The column was in equilibrium with buffer solution (10 mM HEPES-NaOH, pH 7.4, 150 mM NaCl, 1 mM DTT). The eluted sample was loaded into a stainless-steel cell with a window size of 1.5 mm (height) by 3.0 mm (width) by 1.0 mm (thickness) with a 0.02-mm-thick quartz glass window and exposed to X-ray and UV-visible light simultaneously to evaluate the sample concentration at the X-ray-exposed position correctly (46). All the conditions and results of SAXS measurement and analysis are summarized in Table 1. Before injection of the sample into the column, 15 images of flow buffer scattering were collected for background data. The scattering intensities recorded on the two-dimensional (2D) image were azimuthally averaged to convert the one-dimensional (1D) profile and were subtracted from the background intensities using SAnGler (47). We observed no effect of radiation damage under these conditions of the solution flow rate and the exposure time. The conversion of intensities to an absolute scale was performed using water scattering as a standard. Because no concentration dependence was observed across the entire data, the five data points around the peak derived from each sample were averaged as the final scattering data. The Guinier analyses were performed using autorg of ATSAS (48) under the condition of  $q \times R_g < 1.3$ . The plots in Fig. 3 were drawn by using Igor Pro 8 (WaveMetrics Inc.).

**Zinc identification in MeV-V.** The presence of zinc ions was analyzed by scanning the XAFS. Protein samples were concentrated to 1 mg/ml and mounted on a loop designated for protein crystallography. Wavelength scanning between 1.27 and 1.3 Å was performed at the BL-1A Photon Factory (Tsukuba,



Japan) to observe X-ray fluorescence using an XR-100CR Si-PIN X-ray detector (Amptek). The values of the absorption edges were estimated by CHOOCH (49) from the fluorescence data.

**ITC.** The thermodynamic parameters for the binding between each MeV-V and STAT molecule were determined using isothermal titration calorimetry (ITC) (MicroCal iTC200; Malvern Instruments, Westborough, MA, USA). All samples were dialyzed in ITC buffer (10 mM Na<sub>2</sub>P<sub>6</sub>, pH 7.4, 50 mM NaCl, 1.5 mM TCEP) for 48 h at 4°C. The cell and syringe were filled with 10 μM STAT (U-STAT1, pY-STAT1, STAT2, or STAT2-core) and 100 μM titrants (MeV-V, MeV-V<sub>NT</sub>, MeV-V<sub>ΔN-CT</sub>, or IRF9-IAD). Each experiment consisted of a single 4-μl injection over 4 s of the titrant into the STAT solution at 25°C. The spacing time was 150 s, the reference power was 5 μcal/s, and the stirring speed was set to 750 rpm. For each experiment, the data for ITC buffer injection into the receptor in the cell were used for blank subtraction. Data analysis was performed with using Origin 5.0 software (Malvern Instruments; OriginLab, Northampton, MA, USA) with a single-site binding model.

**Inhibition and kinetic assay using SPR.** Surface plasmon resonance (SPR) experiments were performed using a BIACore3000 instrument (GE Healthcare). Biotinylated IRF9-IAD, STAT2-core, and bovine serum albumin (BSA) (control protein) were immobilized on the CAP chip (GE Healthcare) on each flow cell. The biotinylated proteins were prepared using EZ-Link NHS-PEG4-biotin (Thermo Fisher Scientific). For biotinylation, the reagent and proteins were mixed and incubated for 30 min at room temperature at a molar ratio of 1 to 1, and the unbound reagent was removed using a HiTrap desalting column (GE Healthcare).

For the inhibition assay, MeV-V and STAT2-core were injected over the immobilized IRF9-IAD or BSA (both at 600 resonance units [RU]) in Biacore buffer A (10 mM HEPES, pH 7.4, 300 mM NaCl, 0.005% Tween 20, 1.5 mM TCEP) at 20°C at 40 μl/min. A 50 nM concentration of STAT2-core or a mixture of 50 nM STAT2-core and a series of MeV-V concentrations (1,000, 2,500, 5,000 nM) was used as the analyte. After each cycle, all the ligand (streptavidin-coupled DNA and biotinylated IRF9-IAD) was removed using regeneration buffer (GE Healthcare). For each data point, the response between the analyte and BSA was used for subtraction.

**Complex formation analysis by size exclusion chromatography.** Purified STAT2-core (final concentration, 4.8 μM), MeV-V (4.8 μM), and IRF9-IAD (4.8 μM), alone or in any combination, were prepared in 100 μl solution with buffer B. We waited 1 h after mixing the proteins and injected the mixture into an S200 10/300 Increase column (GE Healthcare) using an AKTA purifier system (GE Healthcare) at 0.6 ml/min at 10°C. To investigate whether MeV-V protein has the ability to disrupt preassembled STAT2-core/IRF9-IAD, STAT2-core and IRF9-IAD were mixed at a molecular ratio of 1:1. One hour later, an equivalent amount of MeV-V was added and mixed, and then we waited 1 h before performing the injection. The comparisons of the MeV-V/IRF9-IAD 1:1 mixture, MeV, and IRF9-IAD were carried out with a 4.0 μM concentration of each sample. Each of the eluted solutions was fractionated to 200 μl, and 80 μl was concentrated using 80 μl 20% trichloroacetate. After the removal of the trichloroacetate solution and rinsing with acetone, the precipitant was resuspended with SDS-PAGE sample buffer and applied to a 15% polyacrylamide gel. Protein in the gel was stained with CBB G-250 (Wako Chemical).

## ACKNOWLEDGMENTS

The cDNA of MeV-V was a courtesy gift from Yusuke Yanagi, Kyushu University. SEC-MALS experiments were carried out courtesy of Tomohide Saio.

This work was supported in part by the Japan Society for the Promotion of Science Grants-in-Aid for Scientific Research KAKENHI (grant no. 17K07296). This research was also supported by the Platform Project for Supporting Drug Discovery and Life Science Research (Basis for Supporting Innovative Drug Discovery and Life Science Research [BINDS]) from the Agency for Japan Medical Research and Development (AMED) under grant no. 17am0101093j0001, 18am0101093j0002, and 19am0101093j0003; by the Hokkaido University, Global Facility Center (GFC), Pharma Science Open Unit (PSOU), funded by the Ministry of Education, Culture, Sports, Science and Technology (MEXT) under the “Support Program for Implementation of New Equipment Sharing System”; by the Hokkaido University Biosurface Project; and by the Takeda Science Foundation.

We declare that there are no conflicts of interest with the contents of this article.

## REFERENCES

1. Audsley MD, Moseley GW. 2013. Paramyxovirus evasion of innate immunity: diverse strategies for common targets. *World J Virol* 2:57–70. <https://doi.org/10.5501/wjv.v2.i2.57>.
2. Vidal S, Curran J, Kolakofsky D. 1990. A stuttering model for paramyxovirus P mRNA editing. *EMBO J* 9:2017–2022. <https://doi.org/10.1002/j.1460-2075.1990.tb08330.x>.
3. Vidal S, Curran J, Kolakofsky D. 1990. Editing of the Sendai virus P/C mRNA by G insertion occurs during mRNA synthesis via a virus-encoded activity. *J Virol* 64:239–246. <https://doi.org/10.1128/JVI.64.1.239-246.1990>.
4. Jacques JP, Hausmann S, Kolakofsky D. 1994. Paramyxovirus mRNA editing leads to G deletions as well as insertions. *EMBO J* 13:5496–5503. <https://doi.org/10.1002/j.1460-2075.1994.tb06884.x>.
5. Curran J, Kolakofsky D. 1988. Scanning independent ribosomal initiation of the Sendai virus X protein. *EMBO J* 7:2869–2874. <https://doi.org/10.1002/j.1460-2075.1988.tb03143.x>.
6. Curran J, Boeck R, Kolakofsky D. 1991. The Sendai virus P gene expresses both an essential protein and an inhibitor of RNA synthesis by shuffling modules via mRNA editing. *EMBO J* 10:3079–3085. <https://doi.org/10.1002/j.1460-2075.1991.tb07860.x>.

7. Coughlin MM, Beck AS, Bankamp B, Rota PA. 2017. Perspective on global measles epidemiology and control and the role of novel vaccination strategies. *Viruses* 9:11. <https://doi.org/10.3390/v9010011>.
8. Griffin DE. 2010. Measles virus-induced suppression of immune responses. *Immunol Rev* 236:176–189. <https://doi.org/10.1111/j.1600-065X.2010.00925.x>.
9. Radecke F, Billeter MA. 1996. The nonstructural C protein is not essential for multiplication of Edmonston B strain measles virus in cultured cells. *Virology* 217:418–421. <https://doi.org/10.1006/viro.1996.0134>.
10. Schneider H, Kaelin K, Billeter MA. 1997. Recombinant measles viruses defective for RNA editing and V protein synthesis are viable in cultured cells. *Virology* 227:314–322. <https://doi.org/10.1006/viro.1996.8339>.
11. Takeuchi K, Kadota S, Takeda M, Miyajima N, Nagata K. 2003. Measles virus V protein blocks interferon (IFN)- $\alpha/\beta$  but not IFN- $\gamma$  signaling by inhibiting STAT1 and STAT2 phosphorylation. *FEBS Lett* 545:177–182. [https://doi.org/10.1016/S0014-5793\(03\)00528-3](https://doi.org/10.1016/S0014-5793(03)00528-3).
12. Devaux P, von Messling V, Songsunthong W, Springfield C, Cattaneo R. 2007. Tyrosine 110 in the measles virus phosphoprotein is required to block STAT1 phosphorylation. *Virology* 360:72–83. <https://doi.org/10.1016/j.virol.2006.09.049>.
13. Caignard G, Guerbois M, Labernardière J-L, Jacob Y, Jones LM, Wild F, Tangy F, Vidalain P-O, I-MAP TIMP. 2007. Measles virus V protein blocks Jak1-mediated phosphorylation of STAT1 to escape IFN- $\alpha/\beta$  signaling. *Virology* 368:351–362. <https://doi.org/10.1016/j.virol.2007.06.037>.
14. Ramachandran A, Parisien J-P, Horvath CM. 2008. STAT2 is a primary target for measles virus V protein-mediated alpha/beta interferon signaling inhibition. *J Virol* 82:8330–8338. <https://doi.org/10.1128/JVI.00831-08>.
15. Palosaari H, Parisien J-P, Rodriguez JJ, Ulane CM, Horvath CM. 2003. STAT protein interference and suppression of cytokine signal transduction by measles virus V protein. *J Virol* 77:7635–7644. <https://doi.org/10.1128/jvi.77.13.7635-7644.2003>.
16. Chinnakannan SK, Nanda SK, Baron MD. 2013. Morbillivirus V proteins exhibit multiple mechanisms to block type 1 and type 2 interferon signalling pathways. *PLoS One* 8:e57063. <https://doi.org/10.1371/journal.pone.0057063>.
17. Caignard G, Bourai M, Jacob Y, Ti-Map Project I-M, Tangy F, Vidalain P-O, Infection-MAPPING project I-MAP. 2009. Inhibition of IFN- $\alpha/\beta$  signaling by two discrete peptides within measles virus V protein that specifically bind STAT1 and STAT2. *Virology* 383:112–120. <https://doi.org/10.1016/j.virol.2008.10.014>.
18. Yokota S, Saito H, Kubota T, Yokosawa N, Amano K, Fujii N. 2003. Measles virus suppresses interferon- $\alpha$  signaling pathway: suppression of Jak1 phosphorylation and association of viral accessory proteins, C and V, with interferon- $\alpha$  receptor complex. *Virology* 306:135–146. [https://doi.org/10.1016/S0042-6822\(02\)00026-0](https://doi.org/10.1016/S0042-6822(02)00026-0).
19. Karlin D, Longhi S, Receveur V, Canard B. 2002. The N-terminal domain of the phosphoprotein of morbilliviruses belongs to the natively unfolded class of proteins. *Virology* 296:251–262. <https://doi.org/10.1006/viro.2001.1296>.
20. Ohno S, Ono N, Takeda M, Takeuchi K, Yanagi Y. 2004. Dissection of measles virus V protein in relation to its ability to block alpha/beta interferon signal transduction. *J Gen Virol* 85:2991–2999. <https://doi.org/10.1099/vir.0.80308-0>.
21. Fontana JM, Bankamp B, Bellini WJ, Rota PA. 2008. Regulation of interferon signaling by the C and V proteins from attenuated and wild-type strains of measles virus. *Virology* 374:71–81. <https://doi.org/10.1016/j.virol.2007.12.031>.
22. Devaux P, Hudacek AW, Hodge G, Valle JR, McChesney MB, Cattaneo R. 2011. A recombinant measles virus unable to antagonize STAT1 function cannot control inflammation and is attenuated in rhesus monkeys. *J Virol* 85:348–356. <https://doi.org/10.1128/JVI.00802-10>.
23. Devaux P, Priniski L, Cattaneo R. 2013. The measles virus phosphoprotein interacts with the linker domain of STAT1. *Virology* 444:250–256. <https://doi.org/10.1016/j.virol.2013.06.019>.
24. Motz C, Schuhmann KM, Kirchofer A, Moldt M, Witte G, Conzelmann K-K, Hopfner K-P. 2013. Paramyxovirus V proteins disrupt the fold of the RNA sensor MDA5 to inhibit antiviral signaling. *Science* 339:690–693. <https://doi.org/10.1126/science.1230949>.
25. Li T, Chen X, Garbutt KC, Zhou P, Zheng N. 2006. Structure of DDB1 in complex with a paramyxovirus V protein: viral hijack of a propeller cluster in ubiquitin ligase. *Cell* 124:105–117. <https://doi.org/10.1016/j.cell.2005.10.033>.
26. Liston P, Briedis DJ. 1994. Measles virus V protein binds zinc. *Virology* 198:399–404. <https://doi.org/10.1006/viro.1994.1050>.
27. Paterson RG, Leser GP, Shaughnessy MA, Lamb RA. 1995. The paramyxovirus SV5 V protein binds two atoms of zinc and is a structural component of virions. *Virology* 208:121–131. <https://doi.org/10.1006/viro.1995.1135>.
28. Pfaller CK, Conzelmann K-K. 2008. Measles virus V protein is a decoy substrate for I $\kappa$ B kinase alpha and prevents Toll-like receptor 7/9-mediated interferon induction. *J Virol* 82:12365–12373. <https://doi.org/10.1128/JVI.01321-08>.
29. Zimm BH. 1948. The dependence of the scattering of light on angle and concentration in linear polymer solutions. *J Phys Colloid Chem* 52:260–267.
30. Kataoka M, Hagihara Y, Mihara K, Goto Y. 1993. Molten globule of cytochrome c studied by small angle X-ray scattering. *J Mol Biol* 229:591–596. <https://doi.org/10.1006/jmbi.1993.1064>.
31. Erickson HP. 2009. Size and shape of protein molecules at the nanometer level determined by sedimentation, gel filtration, and electron microscopy. *Biol Proced Online* 11:32–51. <https://doi.org/10.1007/s12575-009-9008-x>.
32. Mao X, Ren Z, Parker GN, Sondermann H, Pastorello MA, Wang W, McMurray JS, Demeler B, Darnell JE, Chen X. 2005. Structural bases of unphosphorylated STAT1 association and receptor binding. *Mol Cell* 17:761–771. <https://doi.org/10.1016/j.molcel.2005.02.021>.
33. Soler-Lopez M, Petosa C, Fukuzawa M, Ravelli R, Williams JG, Müller CW. 2004. Structure of an activated Dictyostelium STAT in its DNA-unbound form. *Mol Cell* 13:791–804. [https://doi.org/10.1016/s1097-2765\(04\)00130-3](https://doi.org/10.1016/s1097-2765(04)00130-3).
34. Becker S, Groner B, Müller CW. 1998. Three-dimensional structure of the Stat3 $\beta$  homodimer bound to DNA. *Nature* 394:145–151. <https://doi.org/10.1038/28101>.
35. Chen X, Vinkemeier U, Zhao Y, Jeruzalmi D, Darnell JE, Kuriyan J. 1998. Crystal structure of a tyrosine phosphorylated STAT-1 dimer bound to DNA. *Cell* 93:827–839. [https://doi.org/10.1016/s0092-8674\(00\)81443-9](https://doi.org/10.1016/s0092-8674(00)81443-9).
36. Zhou P, Wagner G. 2010. Overcoming the solubility limit with solubility-enhancement tags: successful applications in biomolecular NMR studies. *J Biomol NMR* 46:23–31. <https://doi.org/10.1007/s10858-009-9371-6>.
37. Hossain MA, Larrous F, Rawlinson SM, Zhan J, Sethi A, Ibrahim Y, Aloï M, Lieu KG, Mok Y-F, Griffin MDW, Ito N, Ose T, Bourhy H, Moseley GW, Gooley PR. 2019. Structural elucidation of viral antagonism of innate immunity at the STAT1 interface. *Cell Rep* 29:1934–1945.e8. <https://doi.org/10.1016/j.celrep.2019.10.020>.
38. Oda K, Matoba Y, Irie T, Kawabata R, Fukushi M, Sugiyama M, Sakaguchi T. 2015. Structural basis of the inhibition of STAT1 activity by Sendai virus C protein. *J Virol* 89:11487–11499. <https://doi.org/10.1128/JVI.01887-15>.
39. Ho J, Pelzel C, Begitt A, Mee M, Elsheikha HM, Scott DJ, Vinkemeier U. 2016. STAT2 is a pervasive cytokine regulator due to its inhibition of STAT1 in multiple signaling pathways. *PLoS Biol* 14:e2000117. <https://doi.org/10.1371/journal.pbio.2000117>.
40. Rengachari S, Groiss S, Devos JM, Caron E, Grandvaux N, Panne D. 2018. Structural basis of STAT2 recognition by IRF9 reveals molecular insights into ISGF3 function. *Proc Natl Acad Sci U S A* 115:E601–E609. <https://doi.org/10.1073/pnas.1718426115>.
41. Martinez-Gutierrez M, Ruiz-Saenz J. 2016. Diversity of susceptible hosts in canine distemper virus infection: a systematic review and data synthesis. *BMC Vet Res* 12:78. <https://doi.org/10.1186/s12917-016-0702-z>.
42. Vuzman D, Levy Y. 2012. Intrinsically disordered regions as affinity tuners in protein-DNA interactions. *Mol BioSyst* 8:47–57. <https://doi.org/10.1039/C1MB05273J>.
43. Baudin F, Müller CW. 2012. JAK-STAT signalling, methods and protocols. *Methods Mol Biol* 967:301–317.
44. Shimizu N, Mori T, Nagatani Y, Ohta H, Saijo S, Takagi H, Takahashi M, Yatabe K, Kosuge T, Igarashi N. 2019. BL-10C, the small-angle X-ray scattering beamline at the photon factory. *AIP Conf Proc* 2054:060041. <https://doi.org/10.1063/1.5084672>.
45. Takagi H, Igarashi N, Nagatani Y, Ohta H, Mori T, Kosuge T, Shimizu N. 2019. New high-brilliance small angle X-ray scattering beamline, BL-15A2 at the photon factory. *AIP Conf Proc* 2054:060038. <https://doi.org/10.1063/1.5084669>.
46. Bernadó P, Shimizu N, Zaccai G, Kamikubo H, Sugiyama M. 2018. Solution scattering approaches to dynamical ordering in biomolecular sys-

- tems. *Biochim Biophys Acta Gen Subj* 1862:253–274. <https://doi.org/10.1016/j.bbagen.2017.10.015>.
47. Shimizu N, Yatabe K, Nagatani Y, Saijyo S, Kosuge T, Igarashi N. 2016. Software development for analysis of small-angle X-ray scattering data. *AIP Conf Proc* 1741:050017. <https://doi.org/10.1063/1.4952937>.
48. Franke D, Petoukhov MV, Konarev PV, Panjkovich A, Tuukkanen A, Mertens HDT, Kikhney AG, Hajizadeh NR, Franklin JM, Jeffries CM, Svergun DI. 2017. ATSAS 2.8: a comprehensive data analysis suite for small-angle scattering from macromolecular solutions. *J Appl Crystallogr* 50:1212–1225. <https://doi.org/10.1107/S1600576717007786>.
49. Evans G, Pettifer RF. 2001. CHOOCH: a program for deriving anomalous-scattering factors from X-ray fluorescence spectra. *J Appl Crystallogr* 34:82–86. <https://doi.org/10.1107/S0021889800014655>.
50. Waterhouse A, Bertoni M, Bienert S, Studer G, Tauriello G, Gumienny R, Heer FT, de Beer TAP, Rempfer C, Bordoli L, Lepore R, Schwede T. 2018. SWISS-MODEL: homology modelling of protein structures and complexes. *Nucleic Acids Res* 46:W296–W303. <https://doi.org/10.1093/nar/gky427>.
51. Artimo P, Jonnalagedda M, Arnold K, Baratin D, Csardi G, de Castro E, Duvaud S, Flegel V, Fortier A, Gasteiger E, Grosdidier A, Hernandez C, Ioannidis V, Kuznetsov D, Liechti R, Moretti S, Mostaguir K, Redaschi N, Rossier G, Xenarios I, Stockinger H. 2012. ExpASY: SIB bioinformatics resource portal. *Nucleic Acids Res* 40:W597–W603. <https://doi.org/10.1093/nar/gks400>.
52. Whitten AE, Cai S, Trewella J. 2008. MULCh: modules for the analysis of small-angle neutron contrast variation data from biomolecular assemblies. *J Appl Crystallogr* 41:222–226. <https://doi.org/10.1107/S0021889807055136>.